Distribution of phonon lifetime in Brillouin zone

Atsushi Togo, 1, * Laurent Chaput, 2 and Isao Tanaka 1, 3, 4

¹Center for Elements Strategy Initiative for Structural Materials,
Kyoto University, Sakyo, Kyoto 606-8501, Japan

²Institut Jean Lamour, UMR CNRS 7198, Université de Lorraine,
Boulevard des Aiguillettes, BP 70239, 54506 Vandoeuvre Les Nancy Cedex, France

³Department of Materials Science and Engineering,
Kyoto University, Sakyo, Kyoto 606-8501, Japan

⁴Nanostructures Research Laboratory, Japan Fine Ceramics Center, Atsuta, Nagoya 456-8587, Japan

Lattice thermal conductivities of zincblende- and wurtzite-type compounds with 33 combinations of elements are calculated with the single-mode relaxation-time approximation and linearized phonon Boltzmann equation from first-principles anharmonic lattice dynamics calculations. In 9 zincblende-type compounds, distributions of phonon linewidths (inverse phonon lifetimes) are discussed in detail. The phonon linewidths vary non-smoothly with respect to wave vector, which is explained from the imaginary parts of the self energies. It is presented that detailed combination of phonon-phonon interaction strength and three phonon selection rule is critically important to determine phonon lifetime for these compounds. This indicates difficulty to predict phonon lifetime quantitatively without anharmonic force constants. However it is shown that joint density of states weighted by phonon numbers, which is calculated only from harmonic force constants, can be potentially used for a screening of the lattice thermal conductivity of materials.

I. INTRODUCTION

At temperatures near or above room temperature, the thermal conductivity of non-metallic solids is governed by phonon-phonon collisions, which is an anharmonic phenomenon. Recent progress of computers, numerical algorithms, and methods of first-principles calculations have enabled us to predict anharmonic force constants quantitatively, and it has even become possible to reproduce well the lattice thermal conductivities of compounds using those anharmonic force constants. However a detailed analysis of anharmonicity which is at work to produce the lattice thermal resistivity is still not well investigated.

In this work we performed systematic lattice thermal conductivity calculations for a class of compounds with the zincblende- and wurtzite-type structures for 33 different combinations of chemical elements. These two crystal structures are equivalent in local coordinations and different in their stacking orders. This is similar to the difference between the face-centered cubic and hexagonal close-packed structures.

We mainly focused on the phonon lifetime since we believe that it is the most critical physical property to seek for a mechanism of lattice thermal conduction. In fact the lattice thermal conductivity and phonon lifetimes are related straightforwardly (see Sec. IIB) in the single-mode relaxation-time (SMRT) method, being merely proportional to each others. The results of these calculations are presented in Fig. 1 and Fig. 2.

In Fig. 1 it is found that the differences of the two crystal structures, i.e., the difference in their stacking orders, affects little the lattice thermal conductivities. The same behavior is also observed for the phonon linewidth distributions and phonon density of states which are presented in Appendix G. For the ease of presentation this allows

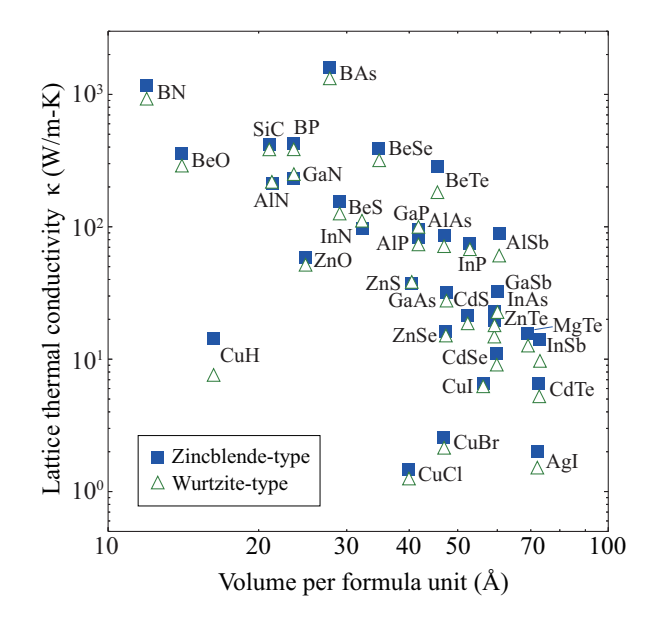


FIG. 1. (color online) Lattice thermal conductivities calculated at 300K with respect to volume per formula unit.

us to focus our discussions only on the zincblende-type compounds. Moreover, since the zincblende-type compound has cubic symmetry, the phonon linewidth distribution in the Brillouin zone will be considered to be nearly isotropic. Therefore the phonon linewidth distributions will mostly be investigated along Γ -L direction.

Fig. 2 shows that a good agreement is obtained with experiments, and evidence the lifetime as an important, controlling, parameter. The lattice thermal conductivities have also be computed from a full solution of the linearized phonon Boltzmann equation (LBTE). As presented in Appendix I, the numerical results, with and

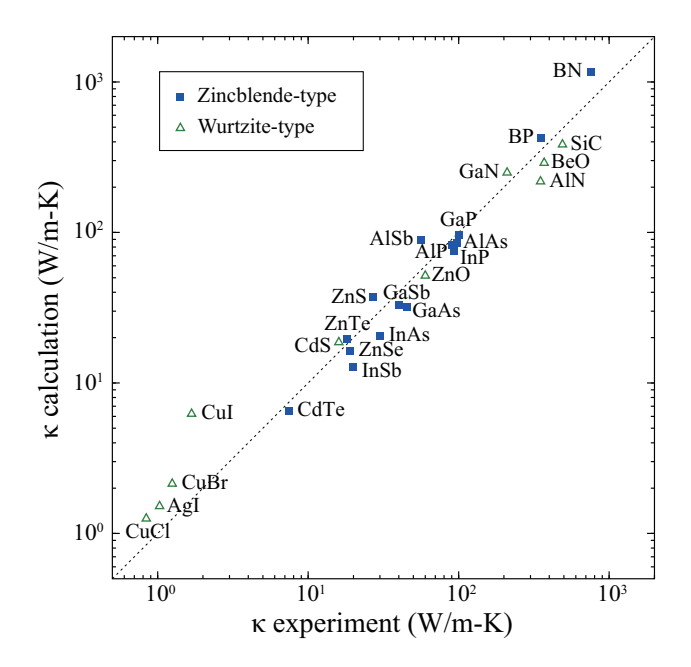


FIG. 2. (color online) Comparison in lattice thermal conductivities at room temperature between experiments and calculations with RTA and witout isotope scattering.

without isotope scattering, are not very much different from those presented in Fig. 1 and Fig. 2. This confirms our claim that the anharmonic lifetime should be understood carefully. Effect of structural disorder, which can vary phonon frequency, linewidth, and lattice thermal conductivity, 14-17 was not considered in this study since the effect is expected to be small for most of these compounds.

The paper is organized as follow. In section II A the method of calculation is reviewed, with the most technical aspects described in Appendix A to E. The results are discussed in section III, which is separated in two parts. In the first part we study the dynamical aspects of the scattering from the (ω, \mathbf{q}) maps of the self energy, and in the second part the average value of the lifetime over the Brillouin zone. The numerical results are collected in Appendix F to I and compared to experiments in Table IV.

II. METHOD OF CALCULATION

A. Phonon lifetime

The phonon lifetime that we discuss in this study is computed from the imaginary part of phonon self energy. The crystal potential is expanded with respect to atomic displacements. The coefficients of the third order which contain the anharmonicity are used to compute the imaginary part of the self energy. For the Hamiltonian \mathcal{H} the expansion can be written as

$$\mathcal{H} = \Phi_0 + \mathcal{T} + \mathcal{H}_2 + \mathcal{H}_3 + \cdots \tag{1}$$

with

$$\mathscr{T} = \frac{1}{2} \sum_{l \kappa \alpha} m_{\kappa} \left[\dot{u}_{\alpha}(l\kappa) \right]^{2}, \tag{2}$$

$$\mathcal{H}_2 = \frac{1}{2} \sum_{l\kappa\alpha} \sum_{l'\kappa'\beta} \Phi_{\alpha\beta}(l\kappa, l'\kappa') u_{\alpha}(l\kappa) u_{\beta}(l'\kappa'), \quad (3)$$

$$\mathcal{H}_{3} = \frac{1}{6} \sum_{l\kappa\alpha} \sum_{l'\kappa'\beta} \sum_{l''\kappa''\gamma} \Phi_{\alpha\beta\gamma}(l\kappa, l'\kappa', l''\kappa'') \times u_{\alpha}(l\kappa)u_{\beta}(l'\kappa')u_{\gamma}(l''\kappa''), \tag{4}$$

where Φ_0 , \mathcal{T} , and \mathcal{H}_n correspond to the constant potential, kinetic energy, and n-body crystal potential terms, respectively. $\mathbf{u}(l\kappa)$ is the atomic displacement of the κ -th atom in the l-th unit cell, m_{κ} is the atomic mass of type κ , and α , β , and γ are the Cartesian indices. $\Phi_{\alpha\beta}$ and $\Phi_{\alpha\beta\gamma}$ denote the harmonic and cubic anharmonic force constants, respectively. The harmonic Hamiltonian is defined as $\mathcal{H}_{\rm H} = \mathcal{T} + \mathcal{H}_2$.

An atomic displacement operator may be written as ¹⁸

$$u_{\alpha}(l\kappa) = \left(\frac{\hbar}{2Nm_{\kappa}}\right)^{\frac{1}{2}} \sum_{\mathbf{q}j} \omega_{\mathbf{q}j}^{-\frac{1}{2}} \left[\hat{a}_{\mathbf{q}j} + \hat{a}_{-\mathbf{q}j}^{\dagger}\right] e^{i\mathbf{q}\cdot\mathbf{r}(l\kappa)} W_{\alpha}(\kappa, \mathbf{q}j)$$

$$(5)$$

where N is the number of unit cells in the crystal and \hbar is the reduced Planck constant. $\mathbf{r}(l\kappa)$ is the equilibrium atomic position and $\hat{a}_{\mathbf{q}j}^{\dagger}$ and $\hat{a}_{\mathbf{q}j}$ are the phonon creation and annihilation operators of the normal mode of band index j and wave vector \mathbf{q} . The harmonic frequency $\omega_{\mathbf{q}j}$ and polarization vector $\mathbf{W}(\kappa, \mathbf{q}j)$ are obtained from the eigenvalue problem of a dynamical matrix $\mathbf{D}(\mathbf{q})$,

$$\sum_{\kappa'\beta} D_{\alpha\beta}(\kappa\kappa', \mathbf{q}) W_{\beta}(\kappa', \mathbf{q}j) = \omega_{\mathbf{q}j}^2 W_{\alpha}(\kappa, \mathbf{q}j), \quad (6)$$

 $_{
m with}$

$$D_{\alpha\beta}(\kappa\kappa', \mathbf{q}) = \frac{1}{\sqrt{m_{\kappa}m_{\kappa'}}} \sum_{l'} \Phi_{\alpha\beta}(0\kappa, l'\kappa') e^{i\mathbf{q} \cdot \left[\mathbf{r}(l'\kappa') - \mathbf{r}(0\kappa)\right]}.$$
(7)

Using Eq. (5) the hamiltonian \mathcal{H} is easily expressed using creation and annihilation operators. We obtain the harmonic part as a sum of harmonic oscillators,

$$\mathcal{H}_{H} = \sum_{\mathbf{q}j} \hbar \omega_{\mathbf{q}j} \left(\frac{1}{2} + \hat{a}_{\mathbf{q}j}^{\dagger} \hat{a}_{\mathbf{q}j} \right), \tag{8}$$

and the third-order potential as a sum of 3-phonon collisions ${\bf r}$

$$\mathscr{H}_{3} = \sum_{\lambda\lambda'\lambda''} \Phi_{\lambda\lambda'\lambda''}(\hat{a}_{\lambda} + \hat{a}_{-\lambda}^{\dagger})(\hat{a}_{\lambda'} + \hat{a}_{-\lambda'}^{\dagger})(\hat{a}_{\lambda''} + \hat{a}_{-\lambda''}^{\dagger}).$$

Here the phonon modes (\mathbf{q}, j) and $(-\mathbf{q}, j)$ have been abbreviated by λ and $-\lambda$, respectively. $\Phi_{\lambda\lambda'\lambda''}$ represent

the strength of interaction between the three phonon λ, λ' and λ' involved in the scattering. $\Phi_{\lambda\lambda'\lambda''}$ is explicitly given by

$$\Phi_{\lambda\lambda'\lambda''} = \frac{1}{\sqrt{N}} \frac{1}{3!} \sum_{\kappa\kappa'\kappa''} \sum_{\alpha\beta\gamma} W_{\alpha}(\kappa,\lambda) W_{\beta}(\kappa',\lambda') W_{\gamma}(\kappa'',\lambda'') \sqrt{\frac{\hbar}{2m_{\kappa}\omega_{\lambda}}} \sqrt{\frac{\hbar}{2m_{\kappa'}\omega_{\lambda'}}} \sqrt{\frac{\hbar}{2m_{\kappa''}\omega_{\lambda''}}} \times \sum_{l'l''} \Phi_{\alpha\beta\gamma}(0\kappa,l'\kappa',l''\kappa'') e^{i\mathbf{q}'\cdot[\mathbf{r}(l'\kappa')-\mathbf{r}(0\kappa)]} e^{i\mathbf{q}''\cdot[\mathbf{r}(l''\kappa'')-\mathbf{r}(0\kappa)]} \times e^{i(\mathbf{q}+\mathbf{q}'+\mathbf{q}'')\cdot\mathbf{r}(0\kappa)} \Delta(\mathbf{q}+\mathbf{q}'+\mathbf{q}'') \tag{10}$$

where $\Delta(\mathbf{q}+\mathbf{q}'+\mathbf{q}'')=1$ when $\mathbf{q}+\mathbf{q}'+\mathbf{q}''$ is a reciprocal lattice vector, and is zero otherwise. In Eqs. (7) and (10) we have used the translational invariance condition to simplify the more symmetric equations which appears in Ref. 18.

The imaginary part of the self energy $\Gamma_{\lambda}(\omega)$ can now be computed up to second order in \mathcal{H}_3 using many body perturbation theory. It takes a form analogous to the Fermi's golden rule,¹⁹

$$\Gamma_{\lambda}(\omega) = \frac{18\pi}{\hbar^2} \sum_{\lambda'\lambda''} \left| \Phi_{-\lambda\lambda'\lambda''} \right|^2 \left\{ (n_{\lambda'} + n_{\lambda''} + 1)\delta(\omega - \omega_{\lambda'} - \omega_{\lambda''}) + (n_{\lambda'} - n_{\lambda''}) \left[\delta(\omega + \omega_{\lambda'} - \omega_{\lambda''}) - \delta(\omega - \omega_{\lambda'} + \omega_{\lambda''}) \right] \right\},$$
(11)

where n_{λ} is the phonon occupation number at the equilibrium,

$$n_{\lambda} = \frac{1}{\exp(\hbar\omega_{\lambda}/k_{\rm B}T) - 1}.$$
 (12)

The double Brillouin zone summation in Eq. (11) is reduced to a single summation due to $\Delta(-\mathbf{q} + \mathbf{q}' + \mathbf{q}'')$ in the calculation.

 $2\Gamma_{\lambda}(\omega_{\lambda})$ corresponds to the phonon linewidth of the phonon mode λ and its reciprocal is known as the phonon lifetime, ¹⁹

$$\tau_{\lambda} = \frac{1}{2\Gamma_{\lambda}(\omega_{\lambda})}.\tag{13}$$

B. Lattice thermal conductivity

When the LBTE is solved under the SMRT method, the lattice thermal conductivity tensor can be written in a closed form, 20

$$\kappa = \frac{1}{NV_0} \sum_{\lambda} C_{\lambda} \mathbf{v}_{\lambda} \otimes \mathbf{v}_{\lambda} \tau_{\lambda}^{\text{SMRT}}, \tag{14}$$

where V_0 is the volume of a unit cell, \mathbf{v}_{λ} and $\tau_{\lambda}^{\mathrm{SMRT}}$ are the group velocity and SMRT of the phonon mode λ , respectively. C_{λ} is the mode dependent heat capacity

defined as

$$C_{\lambda} = k_{\rm B} \left(\frac{\hbar\omega_{\lambda}}{k_{\rm B}T}\right)^2 \frac{\exp(\hbar\omega_{\lambda}/k_{\rm B}T)}{[\exp(\hbar\omega_{\lambda}/k_{\rm B}T) - 1]^2}.$$
 (15)

The group velocity can be obtained directly from the eigenvalue equation (6),

$$v_{\alpha}(\lambda) \equiv \frac{\partial \omega_{\lambda}}{\partial q_{\alpha}}$$

$$= \frac{1}{2\omega_{\lambda}} \sum_{\kappa \kappa' \beta \gamma} W_{\beta}(\kappa, \lambda) \frac{\partial D_{\beta \gamma}(\kappa \kappa', \mathbf{q})}{\partial q_{\alpha}} W_{\gamma}(\kappa', \lambda).$$
(17)

In this study it is further assumed that the phonon relaxation time is given by the phonon lifetime of Eq. (13),

$$\tau_{\lambda}^{\text{SMRT}} \equiv \tau_{\lambda}.$$
 (18)

This is an approximation. Therefore we have also computed the lattice thermal conductivity from a full solution of the LBTE using the method of Ref. 1 which is summarized in Appendix E. Those calculations are much more expensive than the closed expression (14). The results presented in the Appendix I show however that they give thermal conductivities which are numerically quite similar to those with the SMRT approximation for the class of compounds we consider.

C. Computational details

Second- and third-order force constants were obtained by the supercell approach with finite atomic displacements of 0.03 Å. The details of the method are written in Appendix A and in Ref. 21. Non-analytical term correction²² was applied to the second-order force constants to take into account the long range Coulomb forces present in ionic crystals. The technical details to incorporate the non-analytical correction are presented in Appendix B and in Ref. 23.

For the first-principles calculations, we employed the plane-wave basis projector augmented wave method²⁴ within the framework of density functional theory as implemented in the VASP code. 25-27 The generalized gradient approximation (GGA) of Perdew, Burke, and Ernzerhof²⁸ was used for the exchange correlation potential. A plane-wave energy cutoff of 500 eV was employed. Reciprocal spaces of conventional unit cells of the zincblendetype structures and unit cells of the wurtzite-type structures were sampled by $4 \times 4 \times 4$ and $6 \times 6 \times 4$ meshes, respectively. The sampling meshes were shifted from Γ -point by (1/2, 1/2, 1/2) and (0, 0, 1/2) of neighboring mesh grid points along axes, respectively. To obtain atomic forces, the total energies were minimized until the energy convergences to be less than 10^{-8} eV. The lattice parameters of the compounds were optimized under the calculations at zero pressure condition. The results are summarized in Appendix F.

The second-order force constants were computed using $4 \times 4 \times 4$ supercells of the conventional unit cell (512 atoms) for the zincblende-structures and $5 \times 5 \times 3$ supercells for the wurtzite-type structures (300 atoms). Reciprocal spaces of the supercells of the zincblendeand wurtzite-type structures were sampled by $1 \times 1 \times 1$ of Γ -centered meshes and $1 \times 1 \times 2$ meshes shifted by (0,0,1/2) with respect to the grid spacing, respectively. For zincblende-type GaSb, InN, InAs, and InSb, the sampling meshes were shifted by (1/2, 1/2, 1/2) to avoid sampling their Γ -points since their valence and conduction bands slightly touch around the Γ -points due to the underestimation of band gaps by the GGA. Static dielectric constant tensors and Born effective charge tensors were obtained from density functional perturbation theory as implemented in the VASP code. 29,30 These tensors were symmetrized and a sum rule was applied to the Born effective charge tensors following Ref. 31. The phonon band structures and densities of states obtained from those harmonic calculation are presented in Appendix G for all the compounds considered in this study.

For the third-order force constants, $2 \times 2 \times 2$ supercells were built for the zincblende-structures (64 atoms) and $3 \times 3 \times 2$ for the wurtzite-type structures (72 atoms). Reciprocal spaces of the supercells of the zincblende- and wurtzite-type structures were sampled by $2 \times 2 \times 2$ meshes shifted by (1/2, 1/2, 1/2) and (0, 0, 1/2) with respect to the grid spacing, respectively. These anharmonic calculations allow to obtain the lifetimes according to Eq. (11).

The lifetimes for the phonon states of the band structures are shown in Appendix G for all the compounds considered in this study. To obtain those results Brillouin zones were sampled using the $96\times96\times96$ and $80\times80\times48$ sampling meshes for the reciprocal spaces of the primitive cells of the zincblende- and wurtzite-type structures, respectively.

Finally, to compute lattice thermal conductivities, the reciprocal spaces of the primitive cells of the zincblende-and wurtzite-type structures were sampled using the $19\times19\times19$ and $19\times19\times15$ meshes, respectively. In Brillouin zone integrations, crystal symmetry was used to improve numerical accuracy and to reduce the computational cost. A tetrahedron method was employed in the calculation of the imaginary parts of the self energies. $^{32-34}$ The technical details on the Brillouin zone integration are summarized in Appendix C. The computed lattice thermal conductivities are presented in Appendix I.

III. RESULTS AND DISCUSSION

		Group						
		11	12	13	14	15	16	17
	2			В	C	N	0	F
Þ	3			Al	Si	P	S	C1
Period	4	Cu	Zn	Ga	Ge	As	Se	Br
	5	Ag	Cd	In	Sn	Sb	Te	Ι
	6	Au	Hg	Tl	Pb	Bi	Po	At

FIG. 3. (color online) Positions of elements in CuX, ZnX, and GaX on the periodic table.

In this section, we attempt to capture the features how phonons interact in Brillouin zone schematically by limiting our discussion to selected compounds. In Fig. 1, we see a trend that the compounds with larger unit-cell volumes have smaller lattice thermal conductivities. However the copper compounds, CuCl, CuBr, CuI (CuX), clearly ignore this trend. Therefore, to understand this behavior, as shown in Fig. 3, we focus on CuX and their neighbors in the periodic table, ZnS, ZnSe, ZnTe (ZnX) and GaP, GaAs, GaAs (GaX), and compare them to each others to find the characteristics they share. Figures similar to those found in this section are presented in Appendix G and H for all the zincblende-type compounds considered in this study.

The phonon band structures between Γ and L points for CuX, ZnX, and GaX are shown in Fig. 4 from the left column to the right column, respectively. The panels are aligned in relation to the periodic table in Fig. 3. The compounds at the lower panels have heavier anion atoms, therefore as it is expected from Eqs. (6) and (7),

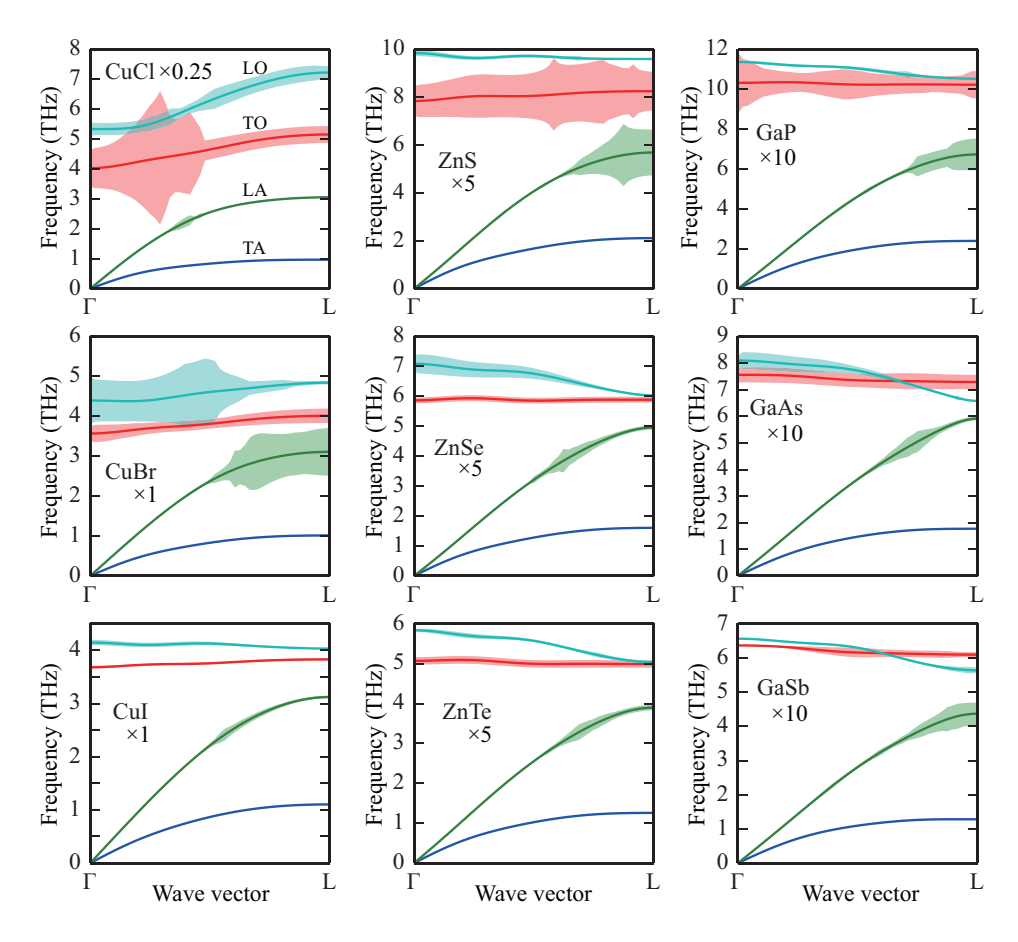


FIG. 4. (color online) Phonon linewidth distributions of CuX, ZnX, and GaX of the zincblende-type structure which are drawn on the phonon band structures between the Γ and L points. The scales of the phonon linewidths and phonon frequencies are shared in THz, but to make the phonon linewidths visible, their magnitudes are adjusted by scale factors (×0.25, ×1, ×5, and ×10) that are shown close to their compound names. Four phonon branches correspond to TA (blue), LA (green), TO (red), and LO (pale blue) modes in order of increasing phonon frequency near Γ -point, respectively.

phonon frequencies become systematically lower in the lower panels. Looking at the panels from left to right, phonon frequencies increase gradually. Therefore, except for CuCl and CuBr, the compounds show rather similar band structures, at different scales. This means that in Eq. (11) the three phonon collisions and decay processes allowed by the conservation laws for energy and momentum will be about the same. Then, if the phonon-phonon interaction strength can be approximated by a function with a simple form, we can expect to analyze those compounds systematically using a small number of parameters.

CuCl and CuBr reveal an interesting behavior. For all compounds there are four phonon branches between Γ and L points. They are labeled as TA (transverse acoustic), LA (longitudinal acoustic), TO (transverse optical), and LO (longitudinal optical) branches in ascending order along vertical axis near Γ point. Usually, acoustic branches have larger dispersion and group velocity than optical branches and the phonon mode frequency of an optical branch is weakly dependent on wave vector. How-

ever CuCl shows relatively large dispersions in the optical branches. In non-metallic crystals, atomic displacements of LO-like phonon modes near Γ point induce a macroscopic electric field. As a result, the phonon mode frequency of an LO branch is lifted up and LO and TO branches split near Γ point. Therefore phonon mode frequency of an LO branch near Γ is higher than that near Brillouin zone boundary in the most compounds. Clear LO-TO splitting is observed in CuCl and CuBr, however the slopes of the LO branches are inverted.

Inverse phonon lifetimes, or linewidths, given in Eq. (13) are drawn on the phonon band structures as the vertical widths of the shaded areas in Fig. 4. Larger linewidth indicates larger phonon scattering and shorter phonon lifetime. The physical unit of THz is shared with phonon mode frequency. To well visualize distributions of the linewidths, the scales of the linewidths are adjusted with multiplying factors. It has to be noticed that phonon lifetimes can be different in logarithmic scale among compounds, which is presumed from the fact that, as shown Fig. 1, lattice thermal conduc-

tivities also range in logarithmic scale. It is found that linewidths vary non-smoothly with respect to wave vector. Partly, this come from the conservation laws for energy and momentum which select regions where more scattering mechanism are possible. As mentioned before, this would also explain the similarities in lifetime distribution for compounds with similar band structures. This will be described in more details.

A. (\mathbf{q}, ω) map of self energy

To find common features, linewidth distributions in Fig. 4 are observed: linewidths of the TA branches are small compared with the other branches, knot-like distributions are found on the LA branches, and, except for CuCl, the TO branch linewidths are roughly constant. To understand how this variety of the linewidth distributions is obtained, we investigated the frequency and wave vector dependencies of the imaginary parts of the self energies. The result of these calculations for all the zincblende-type compounds considered in this study are collected in Appendix H.

Taking ZnTe as an example, we draw (\mathbf{q}, ω) maps of the imaginary parts of the self energies for the TA, LA, TO, and LO branches. As shown in Fig. 5, they are drawn between Γ and L points for $\omega < 6$ THz. The four branches of phonon band structure are superimposed on the corresponding (\mathbf{q}, ω) maps as solid curves. The linewidth distribution of ZnTe in Fig. 4 is reproduced by collecting $2\Gamma_{\lambda}(\omega)$ values on the solid curves where $\omega = \omega_{\lambda}$, i.e. $2\Gamma_{\lambda}(\omega_{\lambda})$. As a general tendency, it is found that the imaginary part of the self energy is weakly dependent on wave vector, however it varies vividly along frequency.

To see their frequency dependency in detail, the profiles of the (\mathbf{q},ω) maps at L point are plotted in Fig. 6 (a). They are drawn up to $\omega \sim 12$ THz since $2\Gamma_{\lambda}(\omega)$ can be nonzero up to twice the maximum phonon mode frequency due to the term $\delta(\omega-\omega_{\lambda'}-\omega_{\lambda''})$ in Eq. (11). Note that 10 times different scales are used to plot $2\Gamma_{\lambda}(\omega)$ below and above 6 THz in Fig. 6 (a). The profiles in the lower frequency range are much smaller than those in the high frequency range. For each profile, the strongest peak appears at $\omega \sim 10$ THz except for the TA branch. The peaks at $\omega \sim 3.5$ THz are relatively large in the frequency range where the phonon modes exist, $\omega < 6$ THz. The phonon band structure of the LA branch crosses this peak frequency as can be seen clearly in Fig. 5. This causes the knot-like shape of the LA branch linewidth.

These peaks of the profiles are mainly brought about by the three phonon selection rules. In Eq. (11), the energy conservation among three phonons is represented by the δ functions and the conservation of momentum appears in Eq. (10) with the Δ function. To understand the role of the selection rules to imaginary part of self energy, the joint density of states (JDOS) is employed. This function is temperature independent. There are two classes of three phonon scattering events. The collision processes, which correspond to that $\delta(\omega-\omega_{\lambda_1}+\omega_{\lambda_2})$ or $\delta(\omega+\omega_{\lambda_1}-\omega_{\lambda_2})$ in Eq. (11), and the decay processes which correspond to $\delta(\omega-\omega_{\lambda_1}-\omega_{\lambda_2})$. In Ref. 20 they are respectively named class 1 and class 2 events, and we will keep this terminology in the following to label different quantities. For example the JDOS $D_2(\mathbf{q},\omega)$ is defined by the sum of the JDOS of the two classes $D_2^{(1)}(\mathbf{q},\omega)$ and $D_2^{(2)}(\mathbf{q},\omega)$ as

$$D_2(\mathbf{q},\omega) = D_2^{(1)}(\mathbf{q},\omega) + D_2^{(2)}(\mathbf{q},\omega)$$
 (19)

where

$$D_2^{(1)}(\mathbf{q}, \omega) = \frac{1}{N} \sum_{\lambda' \lambda''} \Delta(-\mathbf{q} + \mathbf{q}' + \mathbf{q}'') \times \left[\delta(\omega + \omega_{\lambda'} - \omega_{\lambda''}) + \delta(\omega - \omega_{\lambda'} + \omega_{\lambda''}) \right],$$

for class 1 events and

$$D_2^{(2)}(\mathbf{q}, \omega) = \frac{1}{N} \sum_{\lambda' \lambda''} \Delta(-\mathbf{q} + \mathbf{q}' + \mathbf{q}'')$$
$$\times \delta(\omega - \omega_{\lambda'} - \omega_{\lambda''}),$$

for class 2 events. $D_2(\mathbf{q},\omega)$, $D_2^{(1)}(\mathbf{q},\omega)$, and $D_2^{(2)}(\mathbf{q},\omega)$ are shown in Fig. 6 (b) for point L. The peak positions of the profiles coincide with those of the imaginary parts of the self energies. Moreover $D_2^{(1)}(\mathbf{q},\omega)$ and $D_2^{(2)}(\mathbf{q},\omega)$ cover the low and high frequency ranges, respectively. Therefore it is expected that the class 1 (2) event tends to contribute to the phonon lifetimes of the acoustic (optical) branches.

Comparing Figs. 6 (a) and (b), relative intensities of the profiles are clearly different since phonon-phonon interaction strength and phonon occupation numbers are ignored in the JDOS. If we assume that the scattering of the phonon λ with λ' and λ'' can be averaged over λ' and λ'' then the imaginary part of self energy can be approximated as

$$\widetilde{\Gamma}_{\mathbf{q}j}(\omega) = \frac{18\pi}{\hbar^2} P_{-\mathbf{q}j} N_2(\mathbf{q}, \omega)$$
 (20)

with

$$P_{\mathbf{q}j} = \frac{1}{(3n_a)^2} \sum_{\lambda'\lambda''} \left| \Phi_{\lambda\lambda'\lambda''} \right|^2, \tag{21}$$

$$N_2(\mathbf{q}, \omega) = N_2^{(1)}(\mathbf{q}, \omega) + N_2^{(2)}(\mathbf{q}, \omega)$$
 (22)

and

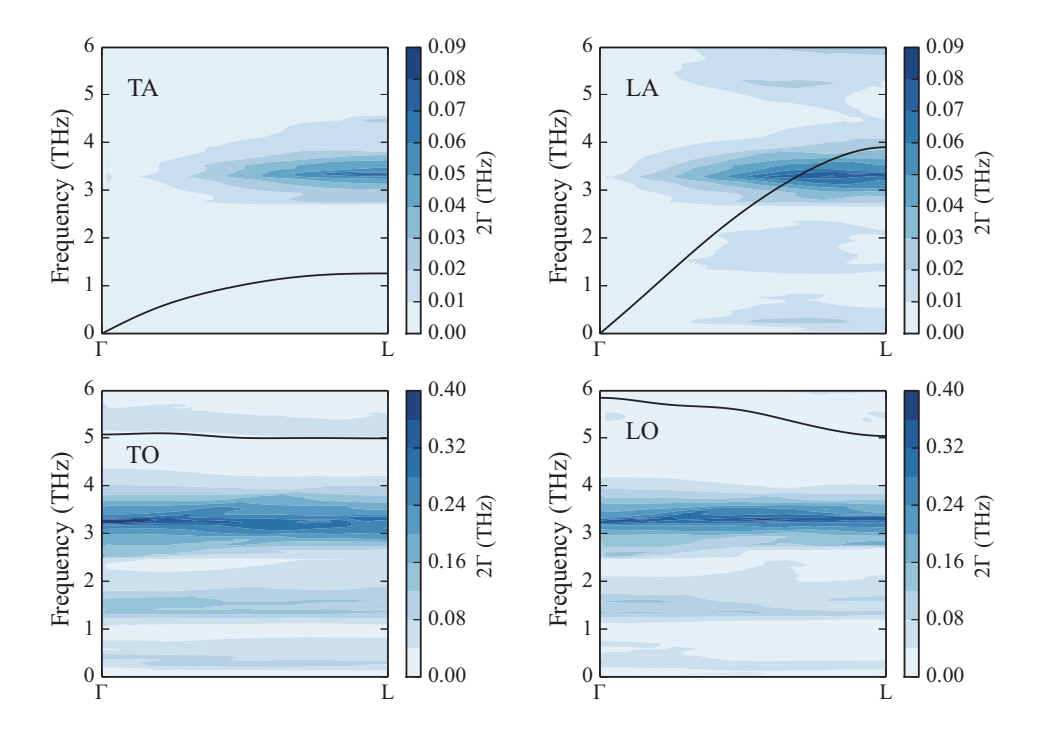


FIG. 5. (color online) Imaginary parts of self energies of ZnTe as functions of wave vector between Γ and L points and frequency at 300 K for TA, LA, TO, and LO branches. Phonon dispersion curves of the corresponding branches are superimposed.

$$N_2^{(1)}(\mathbf{q},\omega) = \frac{1}{N} \sum_{\lambda'\lambda''} \Delta(-\mathbf{q} + \mathbf{q}' + \mathbf{q}'')(n_{\lambda'} - n_{\lambda''}) [\delta(\omega + \omega_{\lambda'} - \omega_{\lambda''}) - \delta(\omega - \omega_{\lambda'} + \omega_{\lambda''})]$$
(23)

$$N_2^{(2)}(\mathbf{q},\omega) = \frac{1}{N} \sum_{\lambda'\lambda''} \Delta(-\mathbf{q} + \mathbf{q}' + \mathbf{q}'')(n_{\lambda'} + n_{\lambda''} + 1)\delta(\omega - \omega_{\lambda'} - \omega_{\lambda''}), \tag{24}$$

where n_a in Eq. (21) is the number of atoms in the primitive cell.

The computational cost of $\widetilde{\Gamma}_{\lambda}(\omega)$ may be much smaller than that of $\Gamma_{\lambda}(\omega)$ if we can avoid the computation of third-order force constants using a good approximation. In Eq. (20), $P_{\mathbf{q}j}$ represents the averaged interaction experienced by phonon $\mathbf{q}j$ while propagating in the medium. $N_2(\mathbf{q},\omega)$ is a weighted JDOS (w-JDOS) which measures the number of those interactions, $N_2^{(1)}(\mathbf{q},\omega)$ of them being of class 1, and $N_2^{(2)}(\mathbf{q},\omega)$ being of class 2.

In Fig. 6 (c), $N_2(\mathbf{q},\omega)$ at L point is presented at 300 K. Below $\omega \sim 2$ THz, the divergence behavior in $D_2^{(1)}(\mathbf{q},\omega)$ has been canceled by the occupation functions in $N_2^{(1)}(\mathbf{q},\omega)$ but the intensity of the peak at $\omega \sim 10$ THz is still comparable to those of the other peaks, which is a noticeable difference with $2\Gamma_{\lambda}(\omega)$. However below $\omega \sim 6$ THz, where the phonon modes do exist, $N_2(\mathbf{q},\omega)$ reasonably reproduces the shapes of the profiles of $2\Gamma_{\lambda}(\omega)$.

One consequence is that $N_2(\mathbf{q}, \omega)$ may be used for a screening of the lattice thermal conductivity of com-

pounds. The (\mathbf{q}, ω) map of $N_2(\mathbf{q}, \omega)$ for ZnTe is shown in Fig. 7. The phonon band structure is superimposed on this (\mathbf{q}, ω) map. The intensity distribution is reasonably similar to those of the imaginary parts of the self energies in Fig. 5. Therefore low (high) lattice thermal conductivity is expected if phonon band structure crosses (avoids) the high intensity region with larger group velocity. Such a discussion for the lattice thermal conductivity will be made elsewhere.

B. Averaged linewidth

To sort the linewidth distributions quantitatively, we define an averaged linewidth over the Brillouin zone, $2\Gamma_{\rm ave}$, as a temporal measure, with

$$\Gamma_{\text{ave}} = \frac{1}{3n_{\text{a}}N} \sum_{\lambda} \Gamma_{\lambda}(\omega_{\lambda}).$$
(25)

Averaged linewidths of CuX, ZnX, and GaX are listed in Table I. The averaged linewidths increase from right

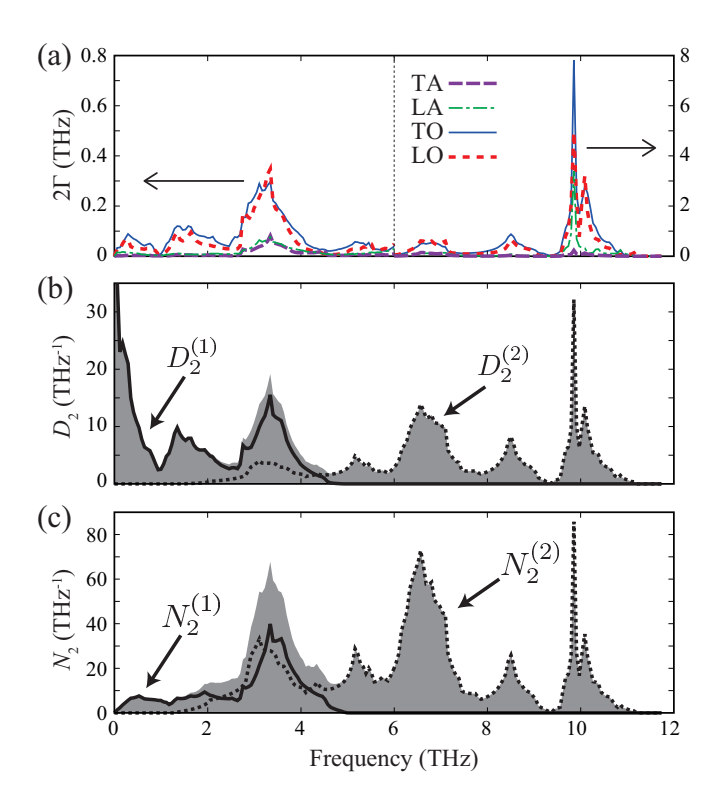


FIG. 6. (color online) Imaginary parts of self energies (2Γ) , JDOS (D_2) , and w-JDOS (N_2) are drawn for ZnTe as a function of phonon frequency at L point. (a) Imaginary parts of self energies 2Γ of TA, LA, TO, and LO branches at 300 K are depicted by dashed, dashed-dotted, solid, and dotted curves, respectively. Note that the scale for the vertical axis is changed below and above 6 THz. (b) JDOS $D_2^{(1)}$ and $D_2^{(2)}$ are drawn by the solid and dotted curves, respectively, and the sum $D_2 = D_2^{(1)} + D_2^{(1)}$ is depicted as the shaded region. (c) w-JDOS $N_2^{(1)}$ and $N_2^{(2)}$ at 300 K are presented by the solid and dotted curves, respectively, and the sum $N_2 = N_2^{(1)} + N_2^{(1)}$ is depicted as the shaded region.

to left and from lower to upper in Table I. Along the compounds with fixed cations, relatively large differences of the averaged linewidths are found between CuBr-CuI and ZnS-ZnSe. We may expect a qualitative change of phonon collisions at these points. The averaged linewidths of the 33 zincblende-type compounds are summarized in Fig. 8 (filled circles). In between BP-BAs, AlAs-AlSb, InP-InAs, and CdS-CdSe, large differences of the averaged linewidths are also found. These qualitative changes are also observed in the linewidth distributions, which are shown in Appendix G.

TABLE I. Averaged linewidths $2\Gamma_{\rm ave}$ of ${\rm Cu}X$, ${\rm Zn}X$, and ${\rm Ga}X$ in THz. See Eq. (25) for the definition of $\Gamma_{\rm ave}$.

CuCl	1.3×10^{0}	ZnS	1.2×10^{-1}	GaP	4.1×10^{-2}
CuBr	4.9×10^{-1}	ZnSe	3.3×10^{-2}	GaAs	2.8×10^{-2}
CuI	3.8×10^{-2}	ZnTe	2.5×10^{-2}	GaSb	1.6×10^{-2}

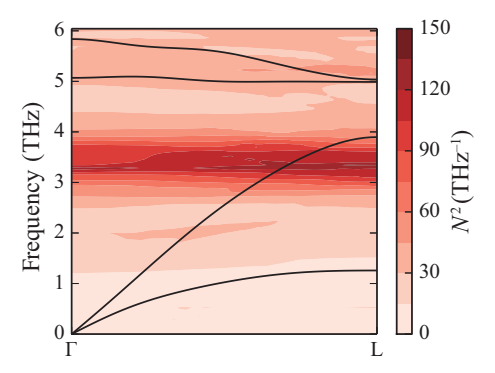


FIG. 7. (color online) w-JDOS (N_2) of ZnTe as functions of wave vector between Γ -L and phonon frequency at 300 K. The solid curves show phonon mode frequencies of the TA, LA, TO, and LO branches in ascending order along the vertical axis

The averaged linewidths obtained with an averaged phonon-phonon interaction, $2\widetilde{\Gamma}_{\rm ave}$ are also shown in Fig. 8 (open circles). $2\widetilde{\Gamma}_{\rm ave}$ tends to overestimate $2\Gamma_{\rm ave}$, however the degree of the overestimation is not systematic among the 33 zincblende-type compounds. This suggests that phonon-phonon interaction strength is as complicated as three phonon selection rule and their detailed combination is decisively important to determine phonon linewidth quantitatively.

IV. SUMMARY

The lattice thermal conductivities of the zincblendeand wurtzite-type compounds with 33 combinations of elements are calculated with RTA and LBTE from firstprinciples anharmonic lattice dynamics calculations. The zincblende- and wurtzite-type compounds with the same compositions show similar lattice thermal conductivities, phonon densities of states, and phonon linewidth distributions though their stacking sequences are different. Focusing on the zincblende-type compounds and selecting CuX, ZnX, and GaX, the phonon linewidth distributions are investigated in detail. It is found that their phonon linewidths are distributed non-smoothly in the Brillouin zones. This is explained by the weak wave vector dependence and the strong frequency dependence of the imaginary parts of the self energies. It is shown that detailed combination of phonon-phonon interaction strength and three phonon selection rule is critically important to determine imaginary part of self energy. Therefore it is considered difficult to predict phonon lifetime quantitatively without a full calculation using anharmonic force constants. However we show a possibility that w-JDOS may be used for a rough estimate of the lattice thermal conductivity and thereby materials screening.

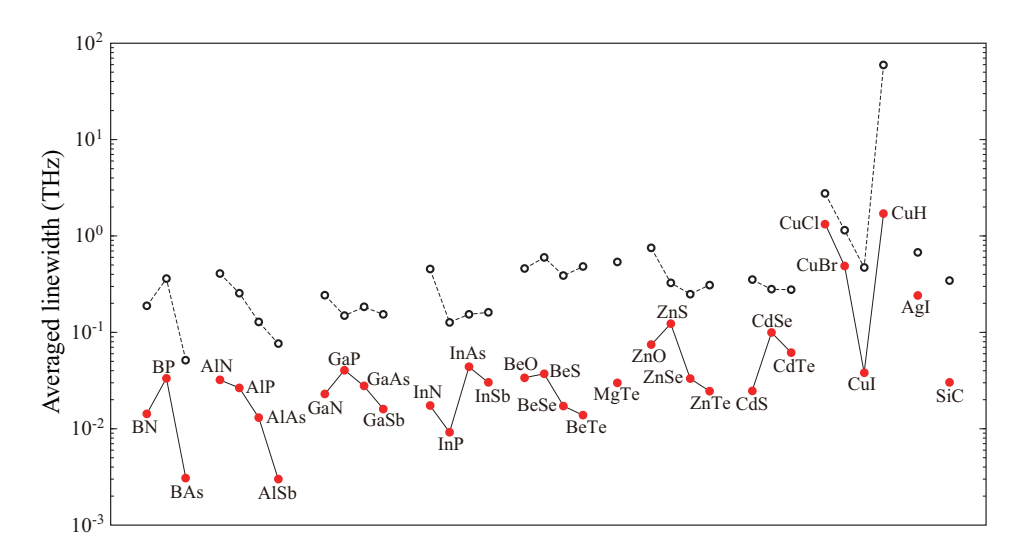


FIG. 8. (color online) Averaged linewidths $2\Gamma_{\rm ave}$ (filled circle) and $2\widetilde{\Gamma}_{\rm ave}$ (open circle) of the 33 zincblende-type compounds. The solid and dashed lines are eye guide to group compounds.

ACKNOWLEDGMENTS

This work was supported by Grant-in-Aid for Scientific Research on Innovative Areas "Nano Informatics" (Grant No. 25106005) from the Japan Society for the Promotion of Science (JSPS), by MEXT Japan through ESISM (Elements Strategy Initiative for Structural Materials) of Kyoto University, by JSPS KAKENHI (Grant No. 26820284), and by a GENCI project under Grant x2014097186.

Appendix A: Supercell approach and finite displacement approach

We employed the supercell approach and the finite displacement approach to calculate force constants. The harmonic and cubic force constants are given by

$$\Phi_{\alpha\beta}(l\kappa, l'\kappa') = \frac{\partial^2 \Phi}{\partial u_{\alpha}(l\kappa)\partial u_{\beta}(l'\kappa')}, \quad (A1)$$

and

$$\Phi_{\alpha\beta\gamma}(l\kappa, l'\kappa', l''\kappa'') = \frac{\partial^3 \Phi}{\partial u_{\alpha}(l\kappa)\partial u_{\beta}(l'\kappa')\partial u_{\gamma}(l''\kappa'')},$$
(A2)

respectively. A set of finite atomic displacements is introduced to supercells to calculate these force constants. Forces acting on atoms in a supercell are obtained from the first-principles calculations and the force constants are calculated from the finite difference method as follows. The harmonic force constants may be approximately obtained by

$$\Phi_{\alpha\beta}(l\kappa, l'\kappa') \simeq -\frac{F_{\beta}[l'\kappa'; \mathbf{u}(l\kappa)]}{u_{\alpha}(l\kappa)}, \tag{A3}$$

where $\mathbf{F}[l'\kappa';\mathbf{u}(l\kappa)]$ is defined as the atomic force measured at $\mathbf{r}(l'\kappa')$ under an atomic displacement $\mathbf{u}(l\kappa)$ in a supercell. The cubic force constants may be similarly obtained by

$$\Phi_{\alpha\beta\gamma}(l\kappa,l'\kappa',l''\kappa'') \simeq -\frac{F_{\gamma}[l''\kappa'';\mathbf{u}(l\kappa),\mathbf{u}(l'\kappa')]}{u_{\alpha}(l\kappa)u_{\beta}(l'\kappa')}, \quad (A4)$$

where $\mathbf{F}[l''\kappa''; \mathbf{u}(l\kappa), \mathbf{u}(l'\kappa')]$ is defined as the atomic force measured at $\mathbf{r}(l''\kappa'')$ under a pair of atomic displacements $\mathbf{u}(l\kappa)$ and $\mathbf{u}(l'\kappa')$ in a supercell. The sets of Eqs. (A3) and (A4) forms systems of linear equations, respectively, and they were solved using the Moore-Penrose pseudoinverse. The computational details are found in Ref. 21.

Configurations of atomic displacements in supercells have to be chosen to solve the linear equations. number of the atomic displacement configurations can be huge, however it may be reduced utilizing crystal symmetry. Atoms that are independent with respect to space group symmetry are selected to be displaced in supercells. The number of displacement directions is reduced using site symmetry at the displaced atom. For the case of cubic force constants, the second atom that is displaced is determined from the symmetry lowered by the first atomic displacement. To gain numerical stability, the opposite direction of a chosen atomic displacement was introduced if they are symmetrically inequivalent. The crystal symmetry is again used to recover full elements of force constants from the reduced set of supercell force calculations. Let a site-symmetry operation S at the displaced atom $\mathbf{r}(l\kappa)$ send an atomic point to the other point as $\mathbf{r}(\tilde{l}'\tilde{\kappa}') \xrightarrow{S} \mathbf{r}(l'\kappa')$. With this site-symmetry operation

and from Eq. (A3), the first atomic displacement, forces on atoms in the supercell, and harmonic force constants are related by

$$\sum_{\alpha\gamma} S_{\alpha\gamma} u_{\gamma}(l\kappa) \Phi_{\alpha\beta}(l\kappa, l'\kappa') \simeq -\sum_{\gamma} S_{\beta\gamma} F_{\gamma}[\tilde{l}'\tilde{\kappa}'; \mathbf{u}(l\kappa)].$$
(A5)

Similarly for the cubic force constants, Eq. (A4) is rewritten as

$$\sum_{\alpha\zeta} S_{\alpha\zeta} u_{\zeta}(l\kappa) \Phi_{\alpha\beta\gamma}(l\kappa, l'\kappa', l''\kappa'') \simeq$$

$$\sum_{\zeta\eta} S_{\beta\zeta} S_{\gamma\eta} \Delta \Phi_{\zeta\eta}[\tilde{l}'\tilde{\kappa}', \tilde{l}''\tilde{\kappa}''; \mathbf{u}(l\kappa)], \quad (A6)$$

where

$$\Delta \Phi_{\beta\gamma}[l'\kappa', l''\kappa''; \mathbf{u}(l\kappa)] \equiv -\frac{F_{\gamma}[l''\kappa''; \mathbf{u}(l\kappa), \mathbf{u}(l'\kappa')]}{u_{\beta}(l'\kappa')} - \Phi_{\beta\gamma}(l'\kappa', l''\kappa''). (A7)$$

Appendix B: Non-analytical term correction

Macroscopic electric field is generated by atomic displacements of phonon modes. At long-wavelength limit, this effect is incorporated as the non-analytical part of harmonic force constants^{22,35,36} given by

$$\Phi_{\alpha\beta}^{\text{na}}(\kappa\kappa',\mathbf{q}) = \frac{4\pi e^2}{V_0} \frac{\sum_{\gamma} q_{\gamma} Z_{\kappa,\gamma\alpha}^* \sum_{\gamma'} q_{\gamma'} Z_{\kappa',\gamma'\beta}^*}{\sum_{\gamma\gamma'} q_{\gamma} \epsilon_{\gamma\gamma'}^{\infty} q_{\gamma'}}, \quad (B1)$$

where e is the elemental charge, Z_{κ}^* is the Born effective charge tensor for the atom κ , and ϵ^{∞} is the high frequency static dielectric constant tensor. The nonanalytical term is ${\bf q}$ dependent but only on its direction in reciprocal space and its application is limited at ${\bf q} \to {\bf 0}$. In the supercell approach, the macroscopic electric field effect at general ${\bf q}$ -points may be included into the dynamical matrix using a Fourier interpolation scheme presented in Ref. 23. The summation in Eq. (7) is made over lattice points in a supercell and the non-analytical term is added to the harmonic supercell force constants divided by the number of unit cells in the supercell, $N_{\rm c}$, as

$$\Phi_{\alpha\beta}^{\text{NAC}}(l\kappa, l'\kappa', \mathbf{q}) = \Phi_{\alpha\beta}(l\kappa, l'\kappa') + \Phi_{\alpha\beta}^{\text{na}}(\kappa\kappa', \mathbf{q})/N_{\text{c}}, \text{ (B2)}$$

which is used instead of normal $\Phi_{\alpha\beta}(l\kappa, l'\kappa')$ to create dynamical matrices in Eq. (7).

In Eq. (16), first derivative of dynamical matrix requires first derivative of the non-analytical term that is

easily obtained as

$$\begin{split} \frac{\partial \Phi^{\mathrm{na}}_{\alpha\beta}(\kappa\kappa',\mathbf{q})}{\partial q_{\zeta}} &= \frac{4\pi e^{2}}{V_{0}} \times \\ &\left[\frac{Z_{\kappa,\zeta\alpha}^{*} \sum_{\gamma'} q_{\gamma'} Z_{\kappa',\gamma'\beta}^{*} + Z_{\kappa',\zeta\beta}^{*} \sum_{\gamma} q_{\gamma} Z_{\kappa,\gamma\alpha}^{*}}{\sum_{\gamma\gamma'} q_{\gamma} \epsilon_{\gamma\gamma'}^{*} q_{\gamma'}} \right. \\ &\left. - \frac{\sum_{\gamma} q_{\gamma} Z_{\kappa,\gamma\alpha}^{*} \sum_{\gamma'} q_{\gamma'} Z_{\kappa',\gamma'\beta}^{*} \sum_{\gamma''} q_{\gamma''} (\epsilon_{\zeta\gamma''}^{\infty} + \epsilon_{\gamma''\zeta}^{\infty})}{\left(\sum_{\gamma\gamma'} q_{\gamma} \epsilon_{\gamma\gamma'}^{\infty} q_{\gamma'}\right)^{2}} \right]. \end{split}$$
 (B3)

Hence the first derivative of the dynamical matrix with the non-analytical term correction becomes

$$\begin{split} &\frac{\partial D_{\alpha\beta}^{\mathrm{NAC}}(\kappa\kappa',\mathbf{q})}{\partial q_{\zeta}} = \frac{1}{\sqrt{m_{\kappa}m_{\kappa}'}} \frac{1}{N_{\mathrm{c}}} \times \\ &\sum_{ll'} \left\{ \frac{1}{N_{\mathrm{c}}} \frac{\partial \Phi_{\alpha\beta}^{\mathrm{na}}(\kappa\kappa',\mathbf{q})}{\partial q_{\zeta}} e^{i\mathbf{q}\cdot\left[\mathbf{r}(l'\kappa')-\mathbf{r}(l\kappa)\right]} + \right. \\ &\left. i\Phi_{\alpha\beta}^{\mathrm{NAC}}(l\kappa,l'\kappa',\mathbf{q}) \left[r_{\zeta}(l'\kappa')-r_{\zeta}(l\kappa)\right] e^{i\mathbf{q}\cdot\left[\mathbf{r}(l'\kappa')-\mathbf{r}(l\kappa)\right]} \right\}. \end{split} \tag{B4}$$

Appendix C: Brillouin zone integration

Computations of phonon lifetimes were discretized using sampling meshes in Brillouin zones. The calculation order of a phonon lifetime in Eq. (11) is $O(n^6)$ with respect to the number of mesh points along an axis. This is reduced using translation symmetry of crystal to $O(n^3)$ by $\Delta(\mathbf{q} + \mathbf{q}' + \mathbf{q}'')$. In Eq. (11), it is supposed that the leftmost index of the phonon-phonon interaction strength (Eq. 10) is fixed and the rest of the indices can be interchanged as $\Phi_{-\lambda\lambda'\lambda''} = \Phi_{-\lambda\lambda''\lambda'}$. Therefore the calculation order becomes $O(n^3/2)$. A set of **q**-point triplets, $\{(\mathbf{q}, \mathbf{q}', \mathbf{q}'') | \mathbf{q}, \mathbf{q}', \mathbf{q}'' \in \text{Brillouin zone}\}$ was thus reduced. The number of the **q**-point triplets was reduced further considering crystallographic point group symmetry and time-reversal symmetry.

We performed the Brillouin zone integration in Eq. (11) using a linear tetrahedron method. ^{32–34} Smearing method is another popular method that is easier to implement in computer programs. In a smearing method, the delta functions are simply replaced by the Gaussian or Lorentzian functions that are normalized so that those integrals become 1. The advantage of the tetrahedron method over the smearing method is that it can be parameter-free. The straightforward application of the tetrahedron method to Eq. (11) requires the translational invariance condition where Eq. (11) is reduced to a single summation over Brillouin zone. ³⁴ By sorting the order of integration of contributions from vertices of tetrahedra, each delta function is simply replaced by respective integration weight that is pre-calculated from phonon mode

frequencies on a sampling mesh.³³ Therefore after computing the integration weights, the tetrahedron method and smearing method can be treated in a computer program on equal footing. Generally the smearing method with an appropriate smearing parameter underestimates phonon lifetime, and thus lattice thermal conductivity as well. In both methods, the integrations are necessary to be performed over the reduced set of \mathbf{q} -points or triplets.

The Brillouin zone integration of Eq. (14) reduces to the integration over an irreducible part of the Brillouin zone (IBZ):

$$\kappa_{\alpha\beta} = \frac{1}{NV_0} \sum_{\mathbf{q} \in IBZ} \frac{1}{p_{\mathbf{q}}} \sum_{j} C_{\mathbf{q}j} \tau_{\mathbf{q}j} \times \sum_{\mathbf{R}} \sum_{\gamma\zeta} R_{\alpha\gamma} R_{\beta\zeta} v_{\gamma}(\mathbf{q}j) v_{\zeta}(\mathbf{q}j), \quad (C1)$$

where R runs the point group operations and $p_{\mathbf{q}}$ is the order of point-group of the \mathbf{q} -vector.

Appendix D: Isotope scattering

The scattering rate for a phonon mode by randomly distributed isotopes is given by the second-order perturbation theory as 37

$$\frac{1}{\tau_{\lambda}^{\text{iso}}(\omega)} = \frac{\pi}{2N} \omega_{\lambda}^{2} \sum_{\lambda'} \delta(\omega - \omega_{\lambda'})$$

$$\times \sum_{\kappa} g_{\kappa} \left| \sum_{\alpha} W_{\alpha}(\kappa, \lambda) W_{\alpha}^{*}(\kappa, \lambda') \right|^{2}, \quad (D1)$$

where g_{κ} is the mass variance parameter. g_{κ} is defined by

$$g_{\kappa} = \sum_{i} f_i (1 - m_{i\kappa}/\bar{m}_{\kappa})^2, \tag{D2}$$

where f_i and $m_{i\kappa}$ are the mole fraction and relative atomic mass of the *i*th isotope, respectively. \bar{m}_{κ} is the average mass given by $\bar{m}_{\kappa} = \sum_{i} f_{i} m_{i\kappa}$. When both of phonon-phonon and phonon-isotope scattering effects were considered in the calculation, we employed the scattering rate given as the sum of them:

$$\frac{1}{\tau_{\lambda}^{\text{total}}} = \frac{1}{\tau_{\lambda}} + \frac{1}{\tau_{\lambda}^{\text{iso}}(\omega_{\lambda})}.$$
 (D3)

Appendix E: Direct solution of linearized phonon Boltzmann equation

Recently the method of the direct solution of the linearized phonon Boltzmann equation was developed by Chaput.¹ In this method, lattice thermal conductivity is given by

$$\kappa_{\alpha\beta} = \frac{\hbar^2}{4k_{\rm B}T^2NV_0} \sum_{\lambda\lambda'} \frac{\omega_{\lambda}v_{\alpha}(\lambda)}{\sinh\left(\frac{\hbar\omega_{\lambda}}{2k_{\rm B}T}\right)} \frac{\omega_{\lambda'}v_{\beta}(\lambda')}{\sinh\left(\frac{\hbar\omega_{\lambda'}}{2k_{\rm B}T}\right)} (\Omega^{\sim 1})_{\lambda\lambda'},$$
(E1)

where $\Omega^{\sim 1}$ denotes the Moore-Penrose inverse of the collision matrix Ω that is given by

$$\Omega_{\lambda\lambda'} = \delta_{\lambda\lambda'} \frac{1}{\tau_{\lambda}} + \frac{\pi}{\hbar^{2}} \sum_{\lambda''} \left| \Phi_{\lambda\lambda'\lambda''} \right|^{2} \frac{1}{\sinh\left(\frac{\hbar\omega_{\lambda''}}{2k_{B}T}\right)} \times \left[\delta(\omega_{\lambda} - \omega_{\lambda}' - \omega_{\lambda}'') + \delta(\omega_{\lambda} - \omega_{\lambda}' + \omega_{\lambda}'') \right]. \quad (E2)$$

To include the phonon-isotope scattering effect in Appendix I, τ_{λ} in Eq. (E2) was replaced by $\tau_{\lambda}^{\rm total}$ of Eq. (D3).

Appendix F: Lattice parameters

Since phonon lifetime is sensitive to lattice parameters, the lattice parameters and volumes of the (conventional) unit cells of the zincblende- and wurtzite-type compounds with 33 combinations of chemical elements used in the present study are listed in Table II.

Appendix G: Phonon band structures

Figures from 9 to 20 show the phonon band structures and distributions of phonon linewidths (left panels) and phonon densities of states (DOS) (right panels) for the zincblende- and wurtzite-type compounds with 33 combinations of elements used in the present study. The reciprocal path of Γ -L of the zincblende-type structure is around twice longer than that of Γ -A of the wurtzite-type structure. The dotted curves in the left panel show the phonon band structure of the zincblende-type compound folded at the middle point between L and Γ points to emphasize the similarity between the phonon band structures of the zincblende- and wurtzite-type compounds. The phonon DOS shaded and drawn by solid curves are those of the zincblende- and wurtzite-type compounds, respectively.

TABLE II. Lattice parameters (Å) and volumes (Å 3) of conventional unit cells of the zincblende- and wurtzite-type structures used in the present study.

	· · · F	<i>J</i>			
	Zinch	olende-type	W	/urtzite	-type
	\overline{a}	Volume	\overline{a}	c	volume
BN	3.63	47.6	2.56	4.22	23.9
BP	4.55	94.0	3.20	5.30	47.0
BAs	4.81	111.1	3.38	5.60	55.5
AlN	4.40	85.2	3.13	5.02	42.5
AlP	5.51	166.9	3.89	6.38	83.5
AlAs	5.73	187.8	4.04	6.64	93.9
AlSb	6.23	242.1	4.40	7.23	121.0
GaN	4.55	94.1	3.22	5.24	47.0
GaP	5.51	166.9	3.88	6.39	83.5
GaAs	5.75	189.9	4.05	6.67	95.0
GaSb	6.22	240.2	4.38	7.21	120.1
InN	5.05	128.9	3.58	5.79	64.4
InP	5.96	211.5	4.21	6.90	105.8
InAs	6.19	236.8	4.37	7.17	118.5
InSb	6.63	291.9	4.68	7.69	146.0
BeO	3.83	56.1	2.71	4.41	28.1
BeS	4.88	115.9	3.44	5.67	58.1
BeSe	5.18	139.2	3.65	6.02	69.7
BeTe	5.67	182.1	4.00	6.59	91.1
MgTe	6.51	276.3	4.61	7.50	138.2
ZnO	4.63	99.2	3.29	5.30	49.6
ZnS	5.45	161.7	3.85	6.31	80.9
ZnSe	5.74	189.2	4.05	6.65	94.7
ZnTe	6.18	236.5	4.36	7.18	118.4
CdS	5.94	209.3	4.20	6.84	104.7
CdSe	6.21	239.2	4.39	7.17	119.7
CdTe	6.63	290.8	4.68	7.67	145.6
CuCl	5.43	159.7	3.82	6.32	79.9
CuBr	5.73	187.7	4.04	6.65	93.9
CuI	6.08	224.8	4.29	7.06	112.4
CuH	4.02	64.9	2.87	4.56	32.5
AgI	6.61	288.8	4.67	7.64	144.3
SiC	4.38	84.0	3.09	5.07	42.0

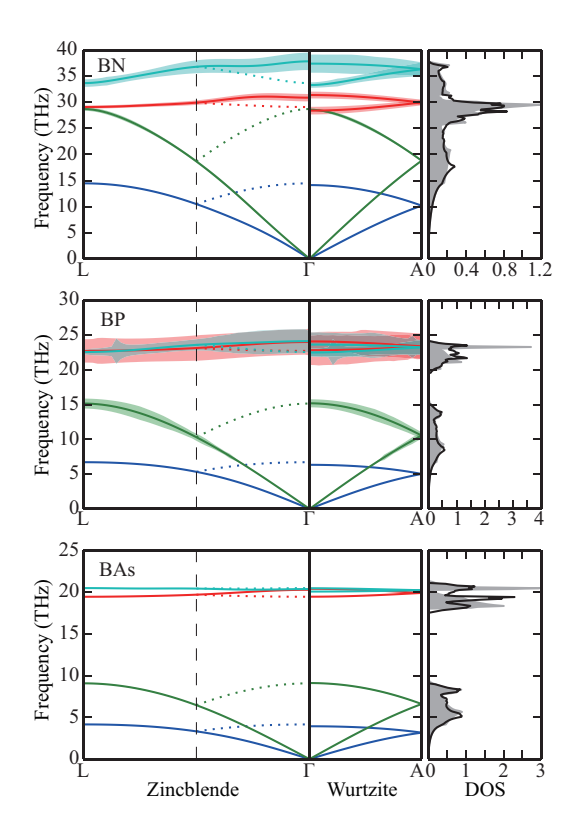


FIG. 9. (color online) Linewidth distributions and phonon densities of states of the zincblende- and wurtzite-type BN, BP, and BAs. The linewidths are drawn by 50 times magnified.

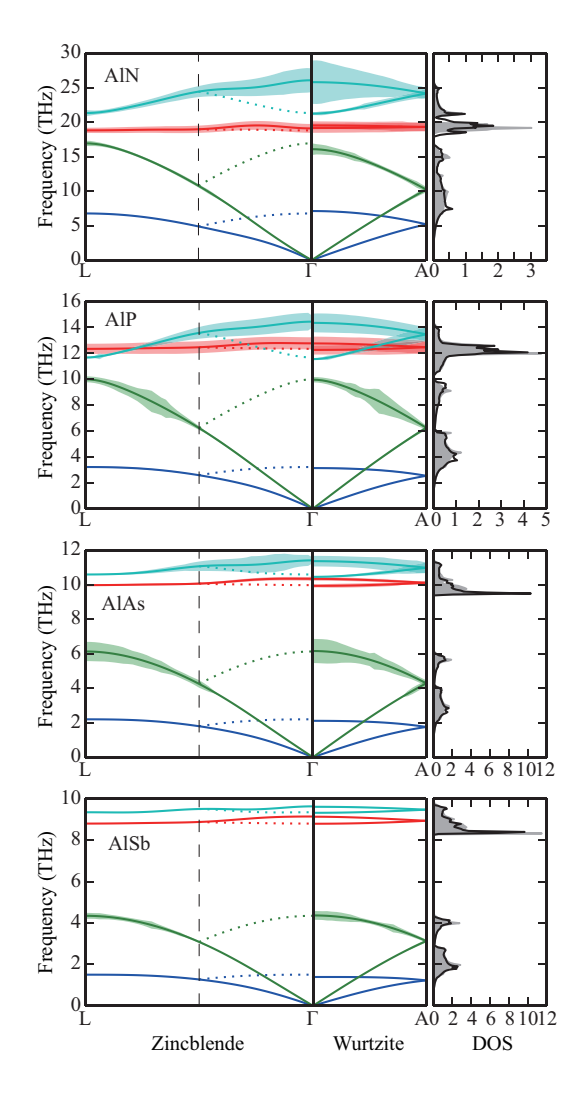


FIG. 10. (color online) Linewidth distributions and phonon densities of states of the zincblende- and wurtzite-type AlN, AlP, AlAs, and AlSb. The linewidths are drawn by 20 times magnified.

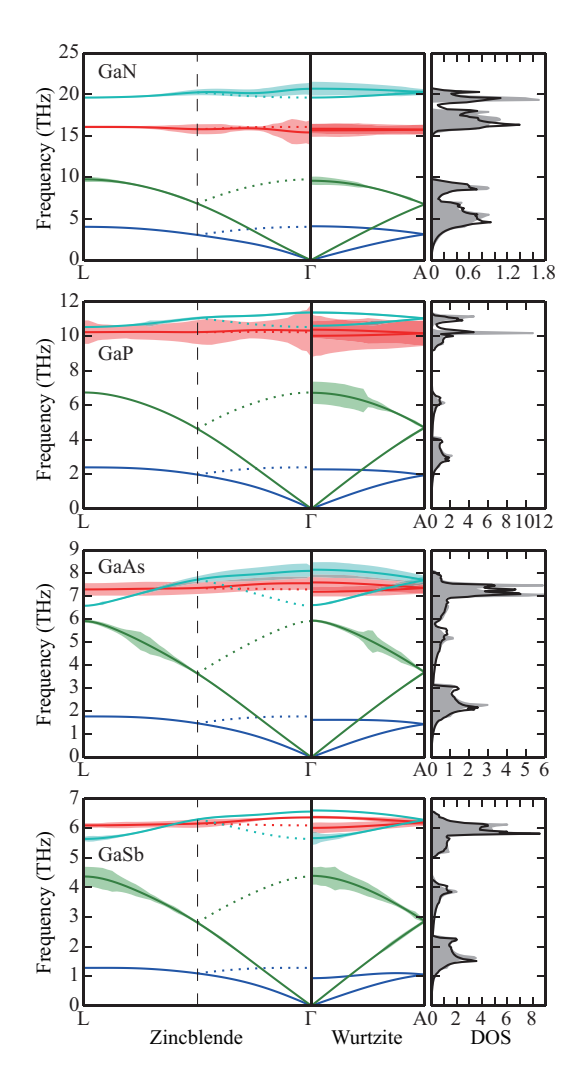


FIG. 11. (color online) Linewidth distributions and phonon densities of states of the zincblende- and wurtzite-type GaN, GaP, GaAs, and GaSb. The linewidths are drawn by 10 times magnified.

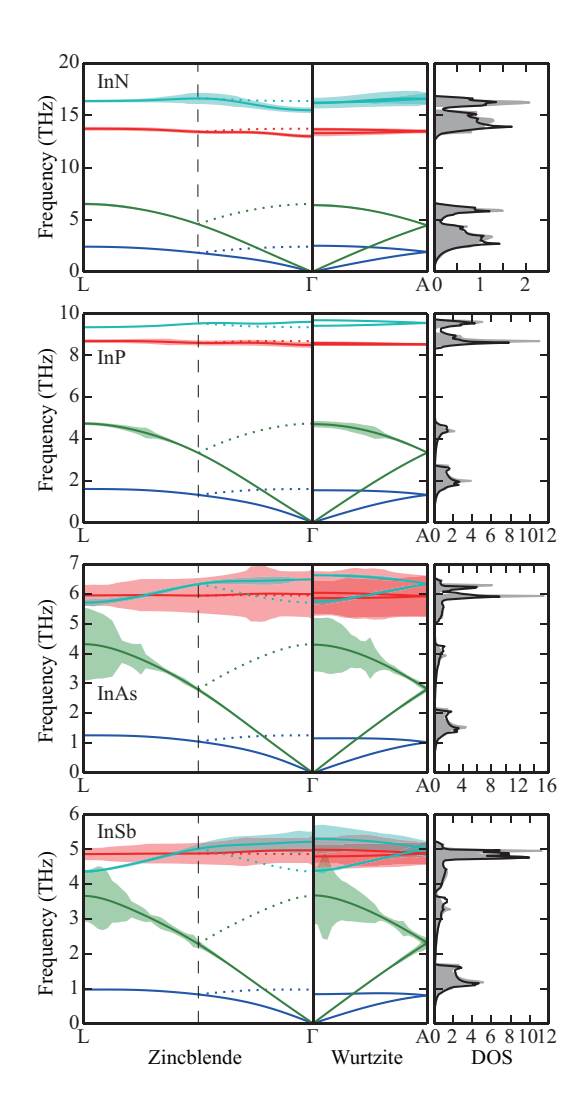


FIG. 12. (color online) Linewidth distributions and phonon densities of states of the zincblende- and wurtzite-type InN, InP, InAs, and InSb. The linewidths are drawn by 10 times magnified.

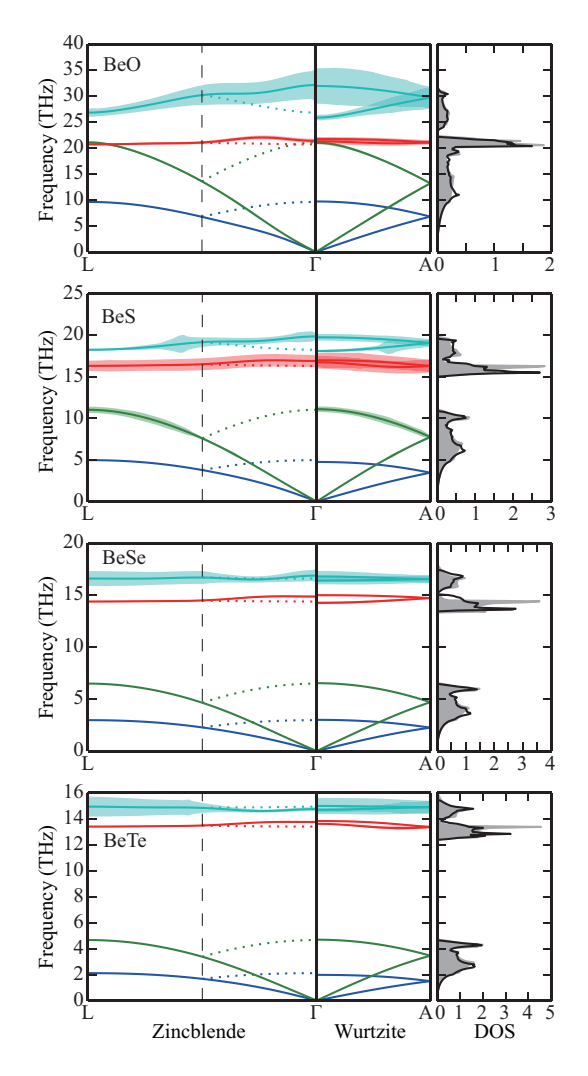


FIG. 13. (color online) Linewidth distributions and phonon densities of states of the zincblende- and wurtzite-type BeO, BeS, BeSe, and BeTe. The linewidths are drawn by 20 times magnified.

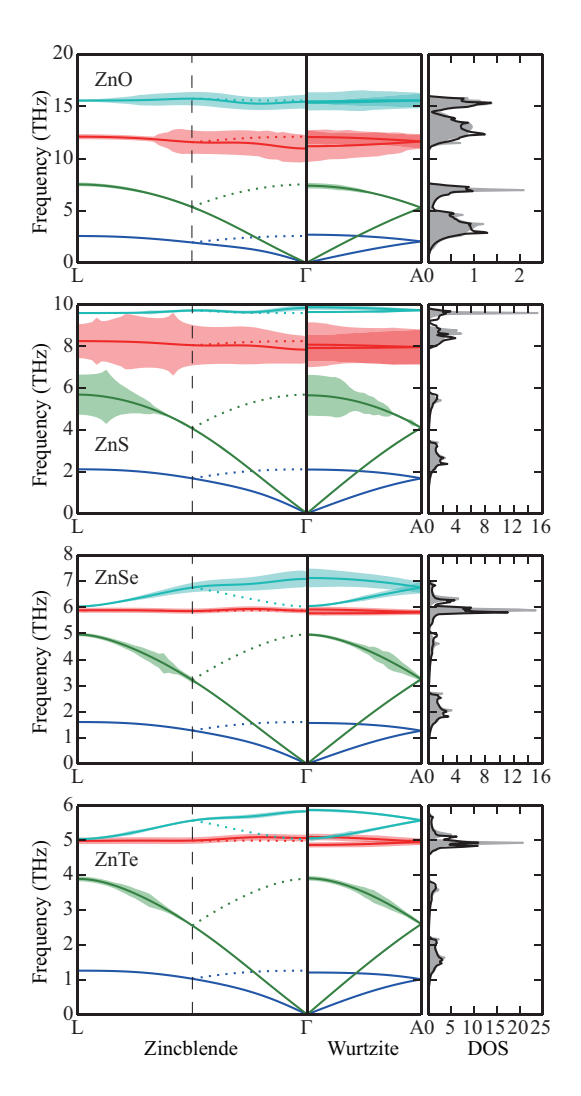


FIG. 15. (color online) Linewidth distributions and phonon densities of states of the zincblende- and wurtzite-type ZnO, ZnS, ZnSe, and ZnTe. The linewidths are drawn by 5 times magnified.

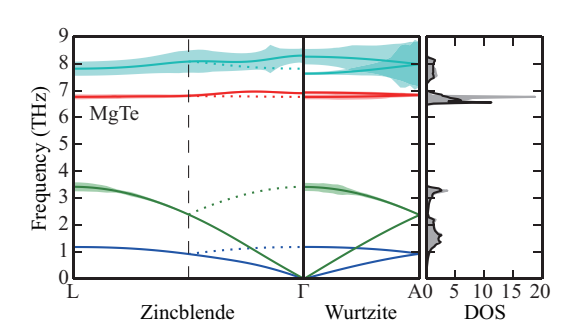


FIG. 14. (color online) Linewidth distributions and phonon densities of states of the zincblende- and wurtzite-type MgTe. The linewidths are drawn by 5 times magnified.

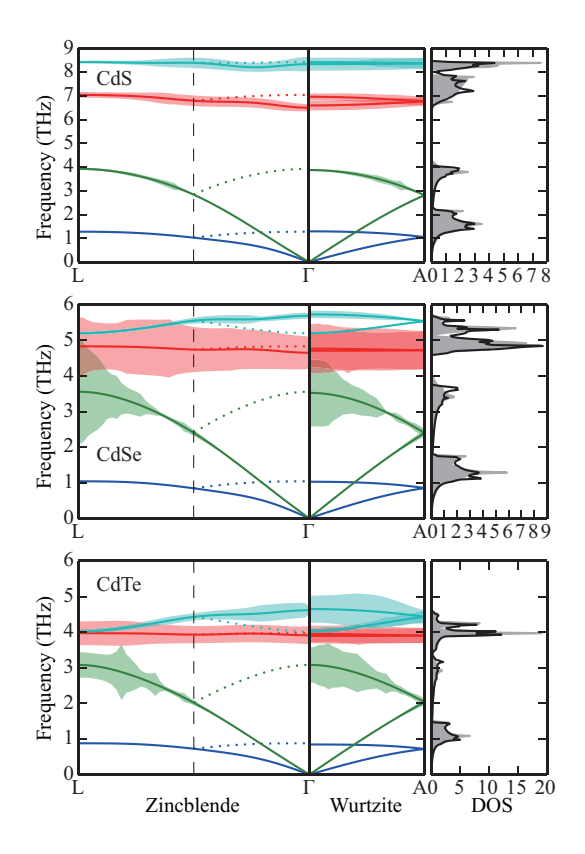


FIG. 16. (color online) Linewidth distributions and phonon densities of states of the zincblende- and wurtzite-type CdS, CdSe, and CdTe. The linewidths are drawn by 5 times magnified.

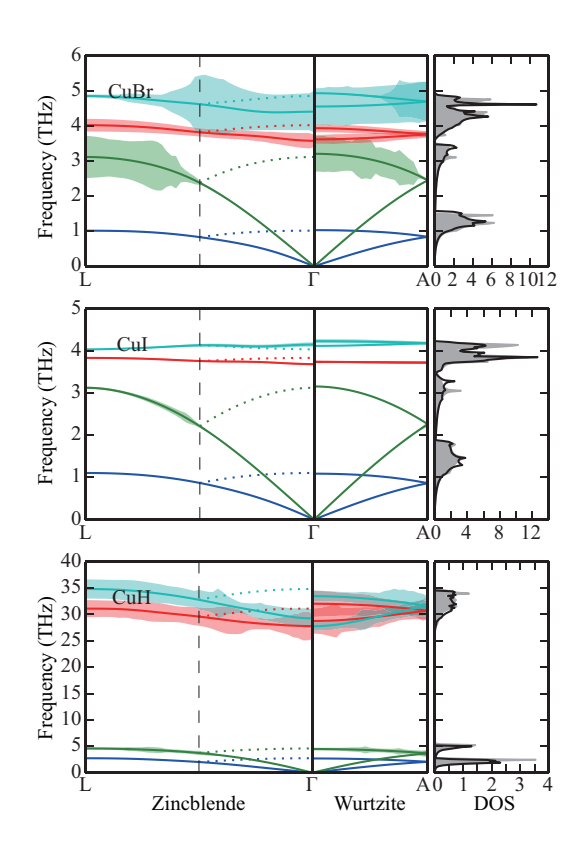


FIG. 18. (color online) Linewidth distributions and phonon densities of states of the zincblende- and wurtzite-type CuBr, CuI, and CuH.

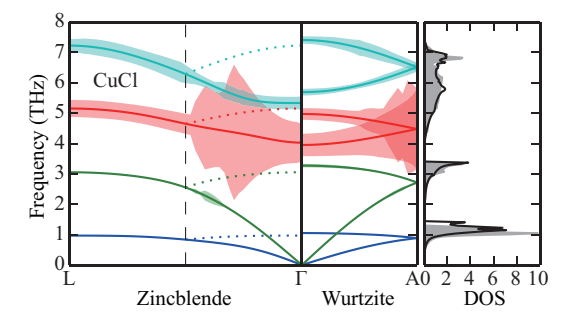


FIG. 17. (color online) Linewidth distributions and phonon densities of states of the zincblende- and wurtzite-type CuCl. The linewidths are drawn by 4 times reduced.

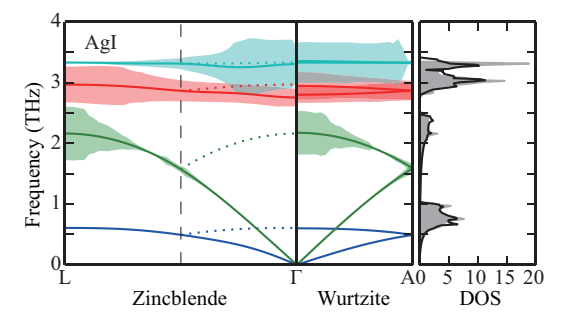


FIG. 19. (color online) Linewidth distributions and phonon densities of states of the zincblende- and wurtzite-type AgI.

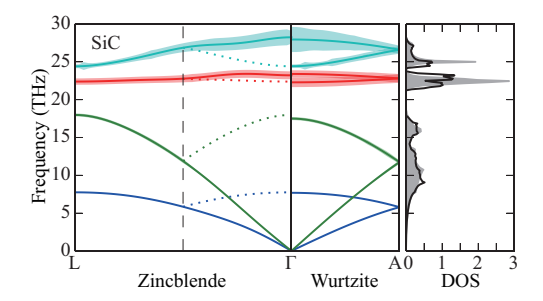


FIG. 20. (color online) Linewidth distributions and phonon densities of states of the zincblende- and wurtzite-type SiC. The linewidths are drawn by 20 times magnified.

Appendix H: Imaginary parts of self energies

Figures from 21 to 53 present (\mathbf{q},ω) maps of imaginary parts of self energies and w-JDOS of the 33 zincblendetype compounds used in the present study. Their phonon band structures are superimposed on the (\mathbf{q},ω) maps.

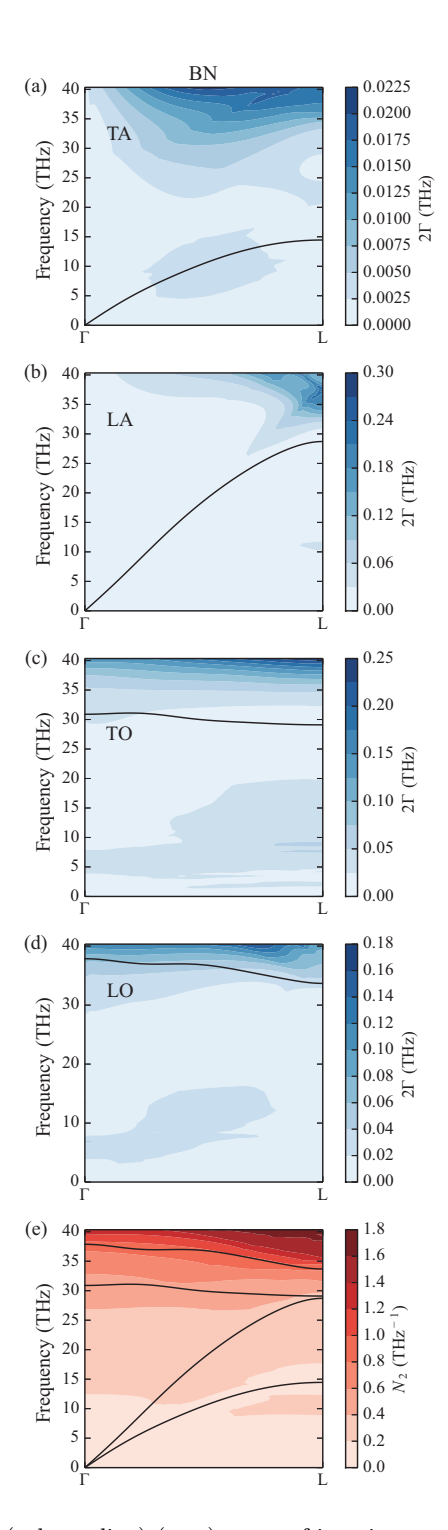


FIG. 21. (color online) (\mathbf{q}, ω) maps of imaginary parts of self energies $2\Gamma_{\lambda}(\omega)$ and w-JDOS $N_2(\mathbf{q}, \omega)$ of BN.

0.045

0.040

0.035

0.030

0.030 0.025 (HZ) 0.020 0.015

0.010

0.005 0.000

> 0.18 0.16

0.14

0.12

0.12 0.10 0.08 0.06

0.04

0.02 0.02

0.40

0.32

0.24 (XHL) 0.16 L7

0.08

 $\Box_{0.00}$ L

0.36

0.32

0.28

0.24

0.08

0.04

30

18 (14Z-18 12 N

0.24 0.20 THL 0.16 TO

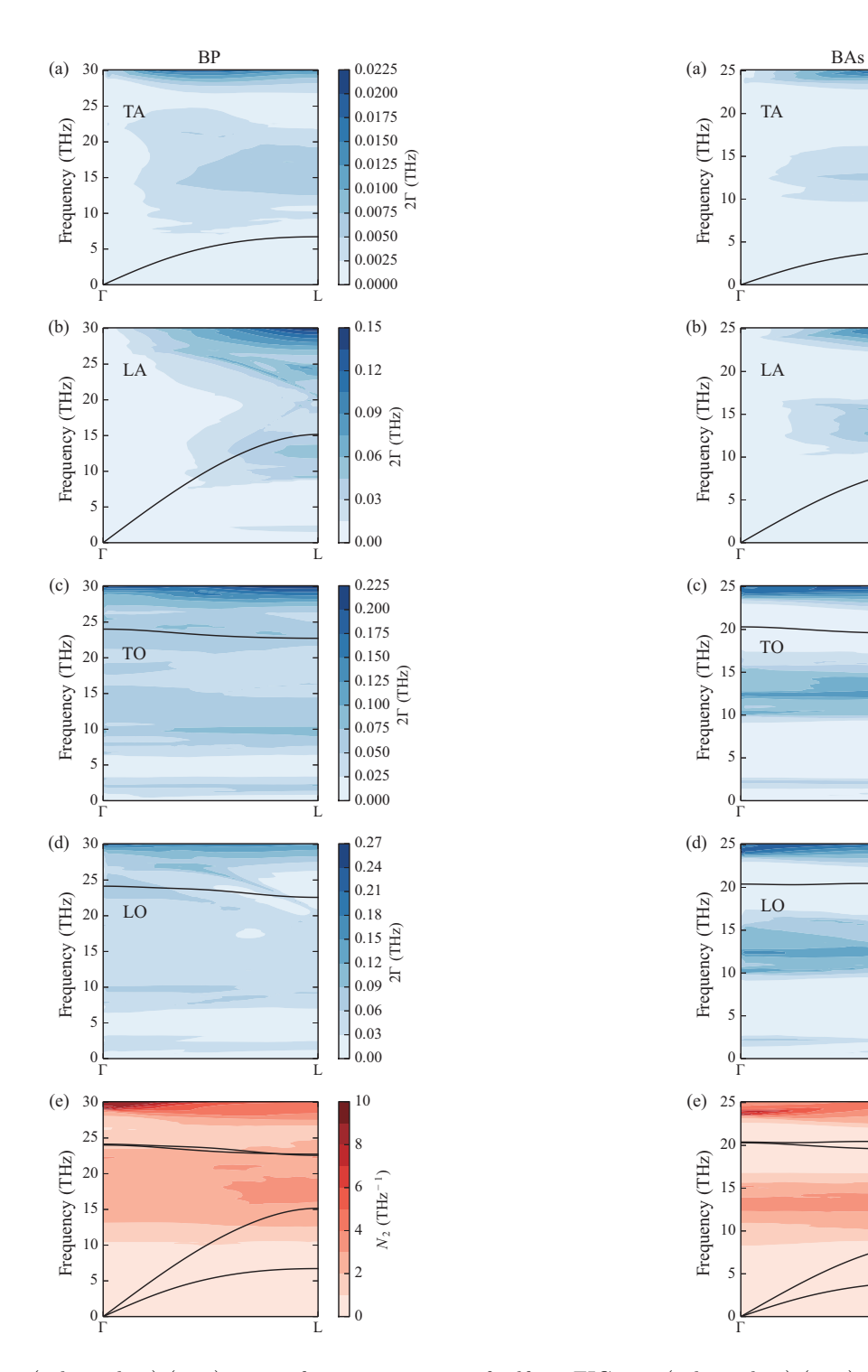


FIG. 22. (color online) (\mathbf{q}, ω) maps of imaginary parts of self energies $2\Gamma_{\lambda}(\omega)$ and w-JDOS $N_2(\mathbf{q},\omega)$ of BP.

FIG. 23. (color online) (\mathbf{q}, ω) maps of imaginary parts of self energies $2\Gamma_{\lambda}(\omega)$ and w-JDOS $N_2(\mathbf{q},\omega)$ of BAs.

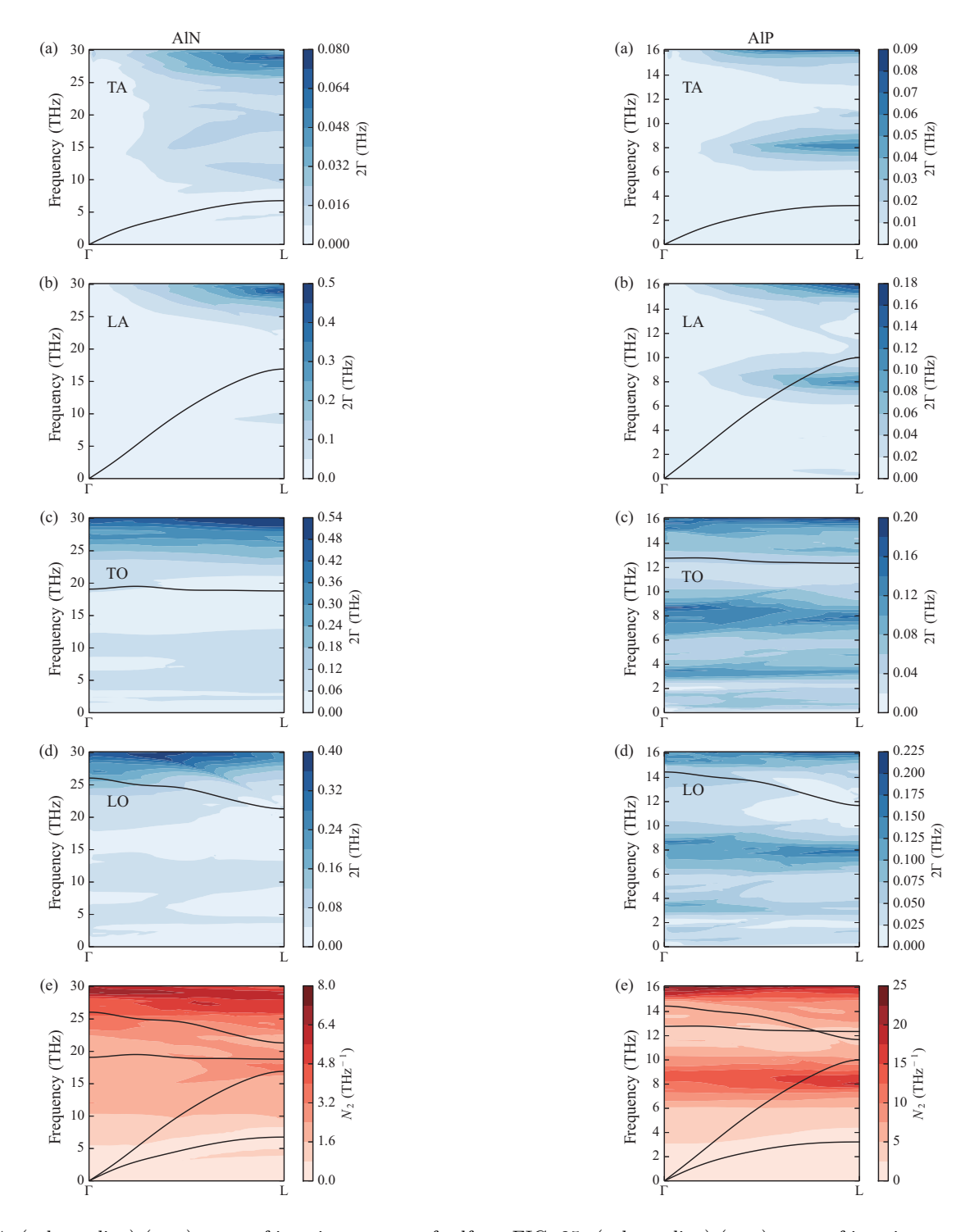


FIG. 24. (color online) (\mathbf{q}, ω) maps of imaginary parts of self energies $2\Gamma_{\lambda}(\omega)$ and w-JDOS $N_2(\mathbf{q}, \omega)$ of AlN.

FIG. 25. (color online) (\mathbf{q}, ω) maps of imaginary parts of self energies $2\Gamma_{\lambda}(\omega)$ and w-JDOS $N_2(\mathbf{q}, \omega)$ of AlP.

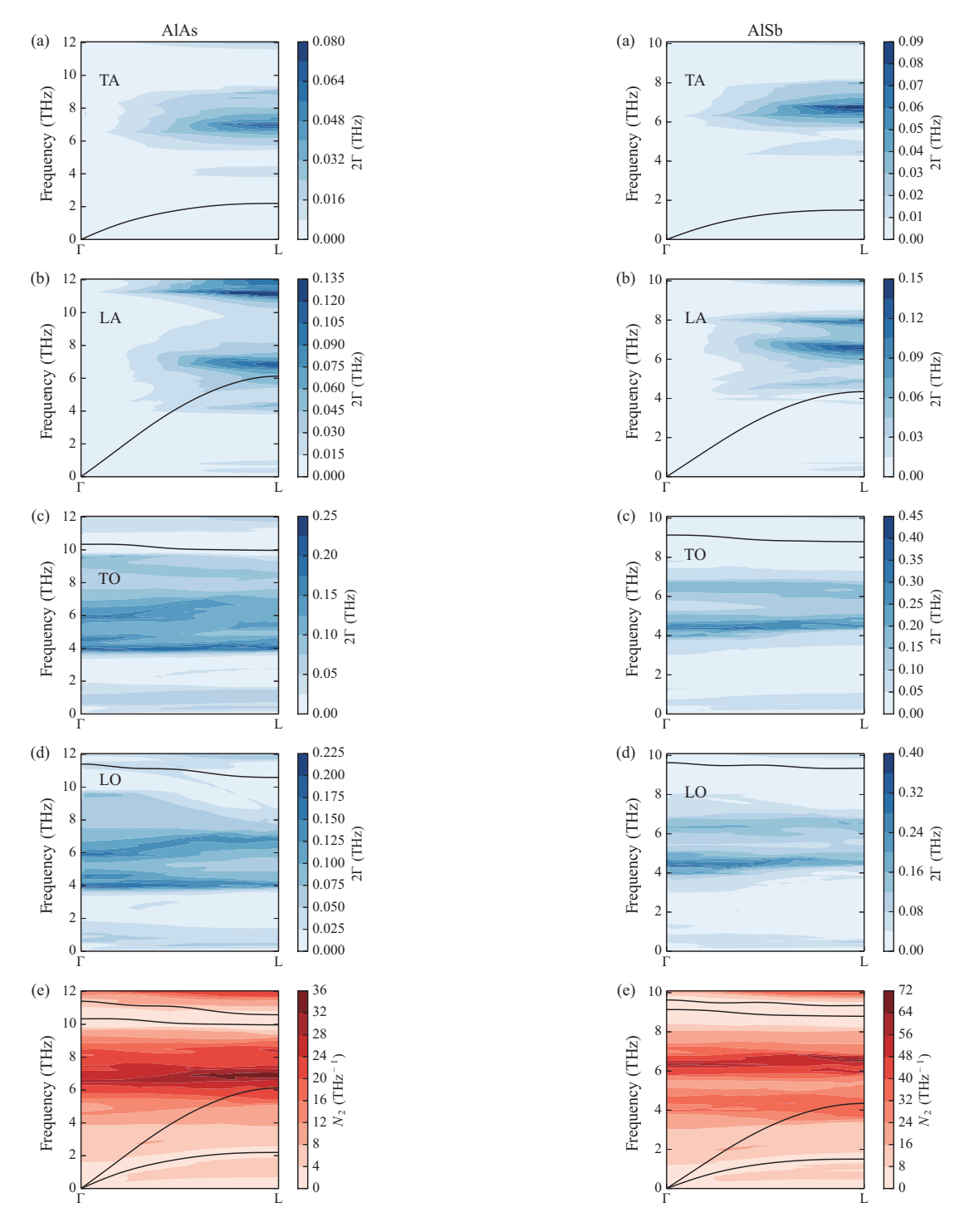


FIG. 26. (color online) (\mathbf{q}, ω) maps of imaginary parts of self energies $2\Gamma_{\lambda}(\omega)$ and w-JDOS $N_2(\mathbf{q}, \omega)$ of AlAs.

FIG. 27. (color online) (\mathbf{q}, ω) maps of imaginary parts of self energies $2\Gamma_{\lambda}(\omega)$ and w-JDOS $N_2(\mathbf{q}, \omega)$ of AlSb.

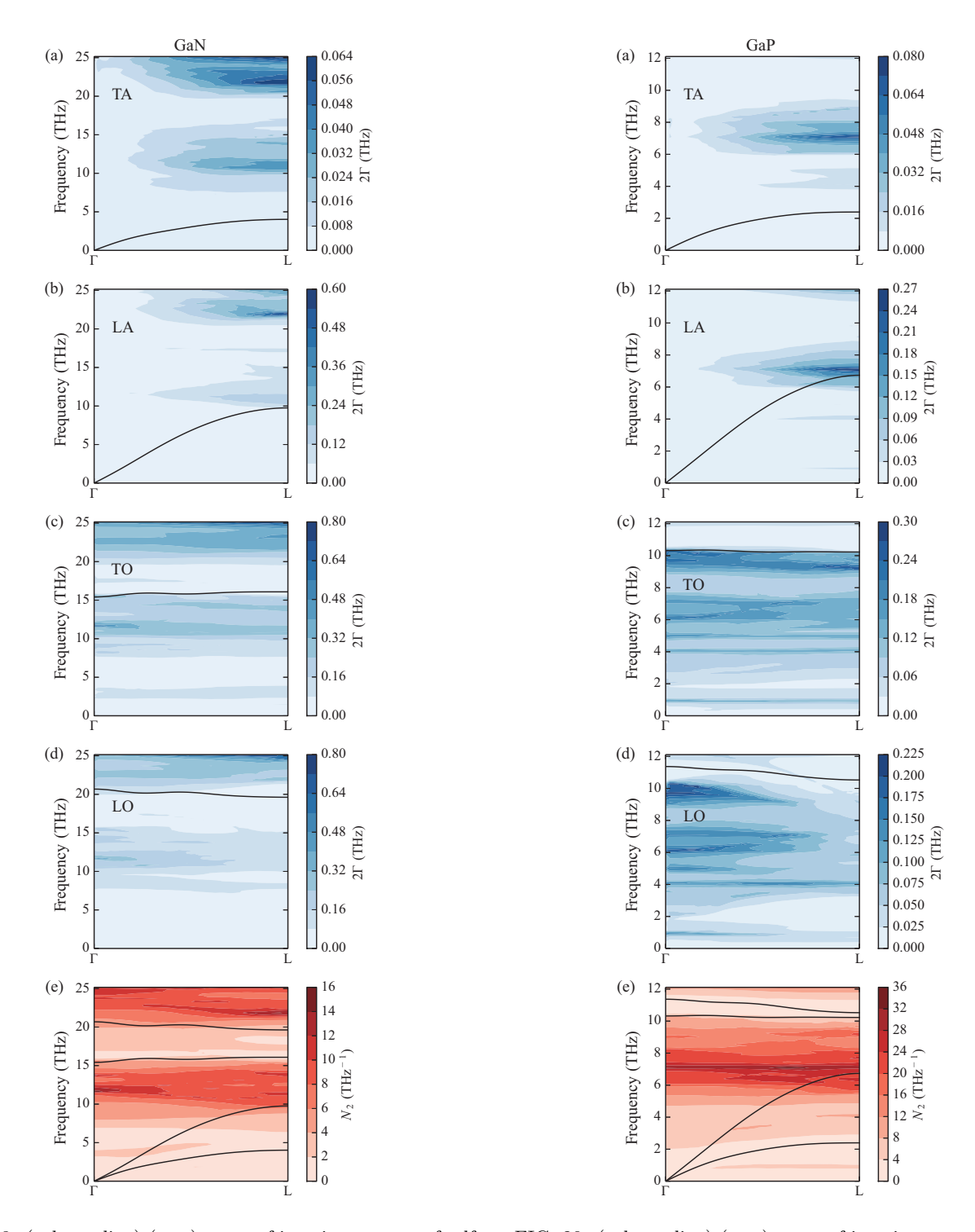


FIG. 28. (color online) (\mathbf{q}, ω) maps of imaginary parts of self energies $2\Gamma_{\lambda}(\omega)$ and w-JDOS $N_2(\mathbf{q}, \omega)$ of GaN.

FIG. 29. (color online) (\mathbf{q}, ω) maps of imaginary parts of self energies $2\Gamma_{\lambda}(\omega)$ and w-JDOS $N_2(\mathbf{q}, \omega)$ of GaP.

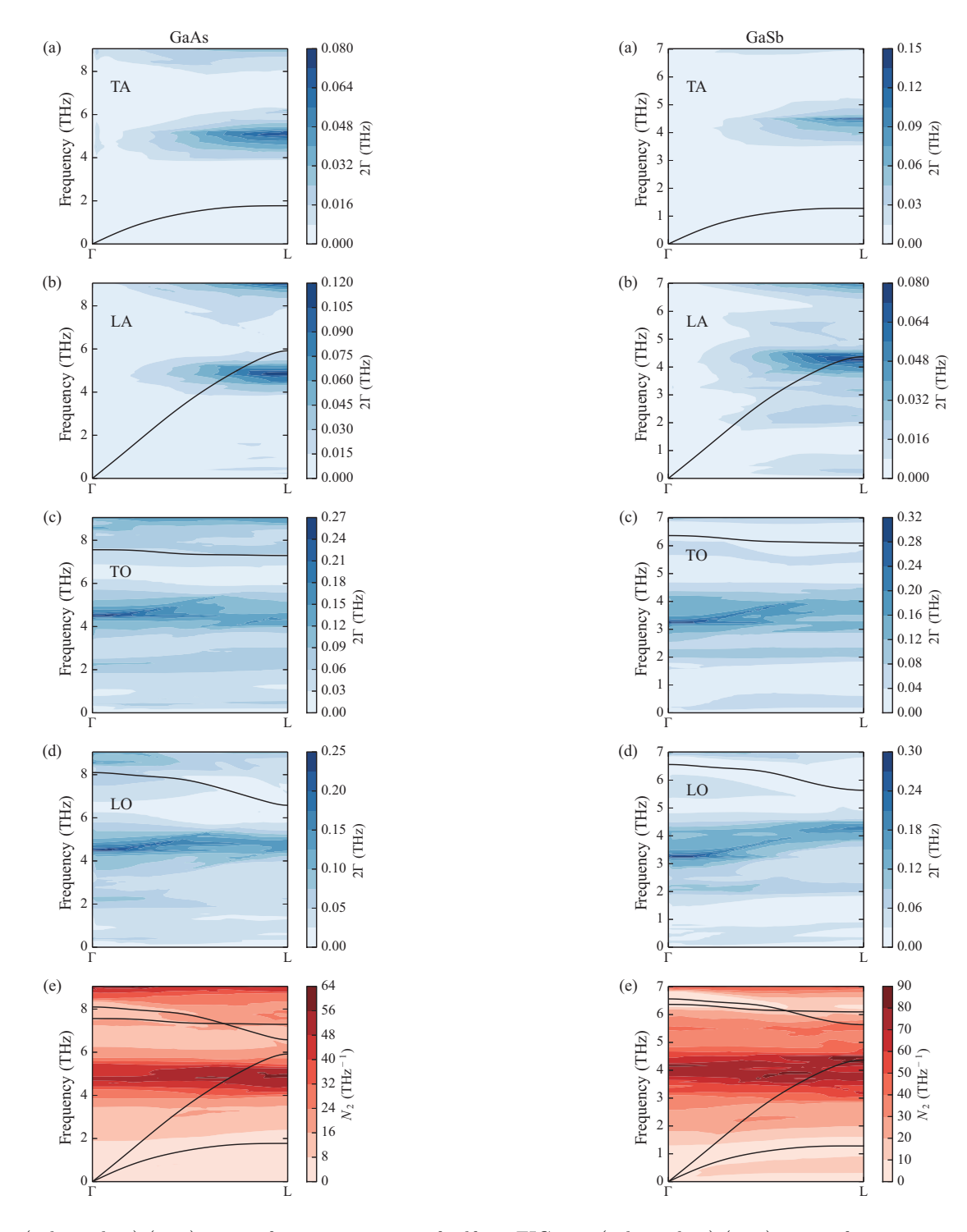


FIG. 30. (color online) (\mathbf{q}, ω) maps of imaginary parts of self energies $2\Gamma_{\lambda}(\omega)$ and w-JDOS $N_2(\mathbf{q}, \omega)$ of GaAs.

FIG. 31. (color online) (\mathbf{q}, ω) maps of imaginary parts of self energies $2\Gamma_{\lambda}(\omega)$ and w-JDOS $N_2(\mathbf{q}, \omega)$ of GaSb.

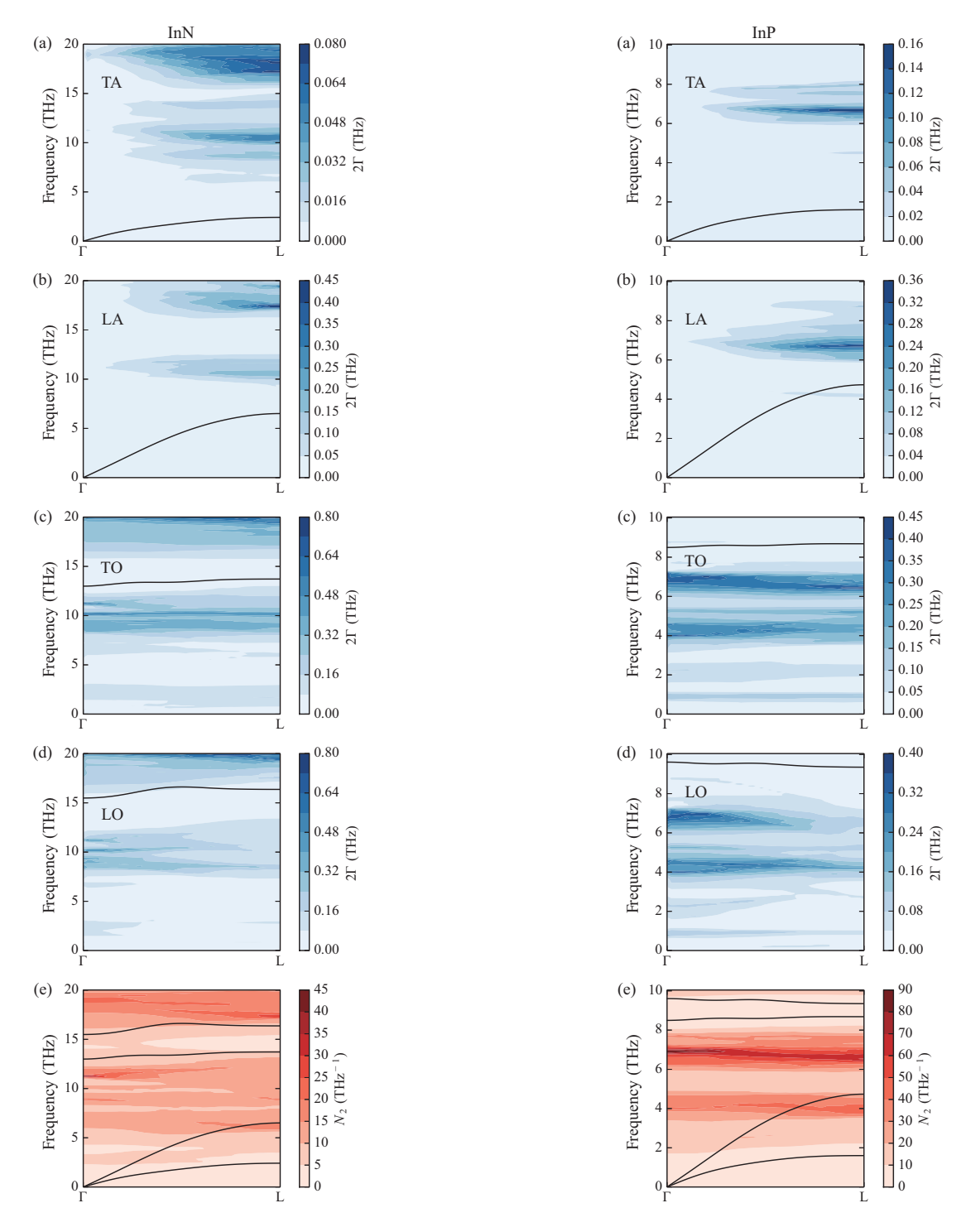


FIG. 32. (color online) (\mathbf{q}, ω) maps of imaginary parts of self energies $2\Gamma_{\lambda}(\omega)$ and w-JDOS $N_2(\mathbf{q}, \omega)$ of InN.

FIG. 33. (color online) (\mathbf{q}, ω) maps of imaginary parts of self energies $2\Gamma_{\lambda}(\omega)$ and w-JDOS $N_2(\mathbf{q}, \omega)$ of InP.

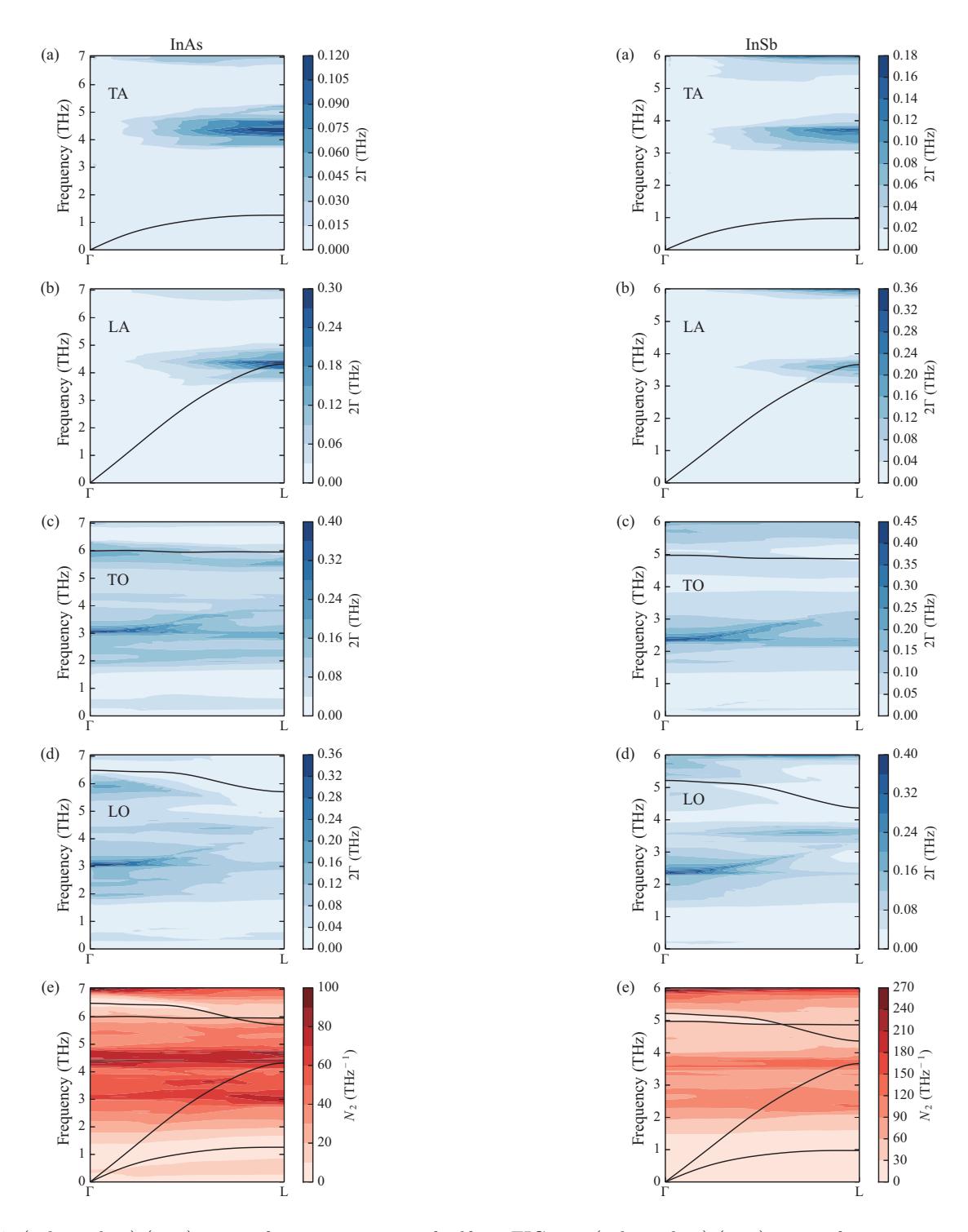


FIG. 34. (color online) (\mathbf{q}, ω) maps of imaginary parts of self energies $2\Gamma_{\lambda}(\omega)$ and w-JDOS $N_2(\mathbf{q}, \omega)$ of InAs.

FIG. 35. (color online) (\mathbf{q}, ω) maps of imaginary parts of self energies $2\Gamma_{\lambda}(\omega)$ and w-JDOS $N_2(\mathbf{q}, \omega)$ of InSb.

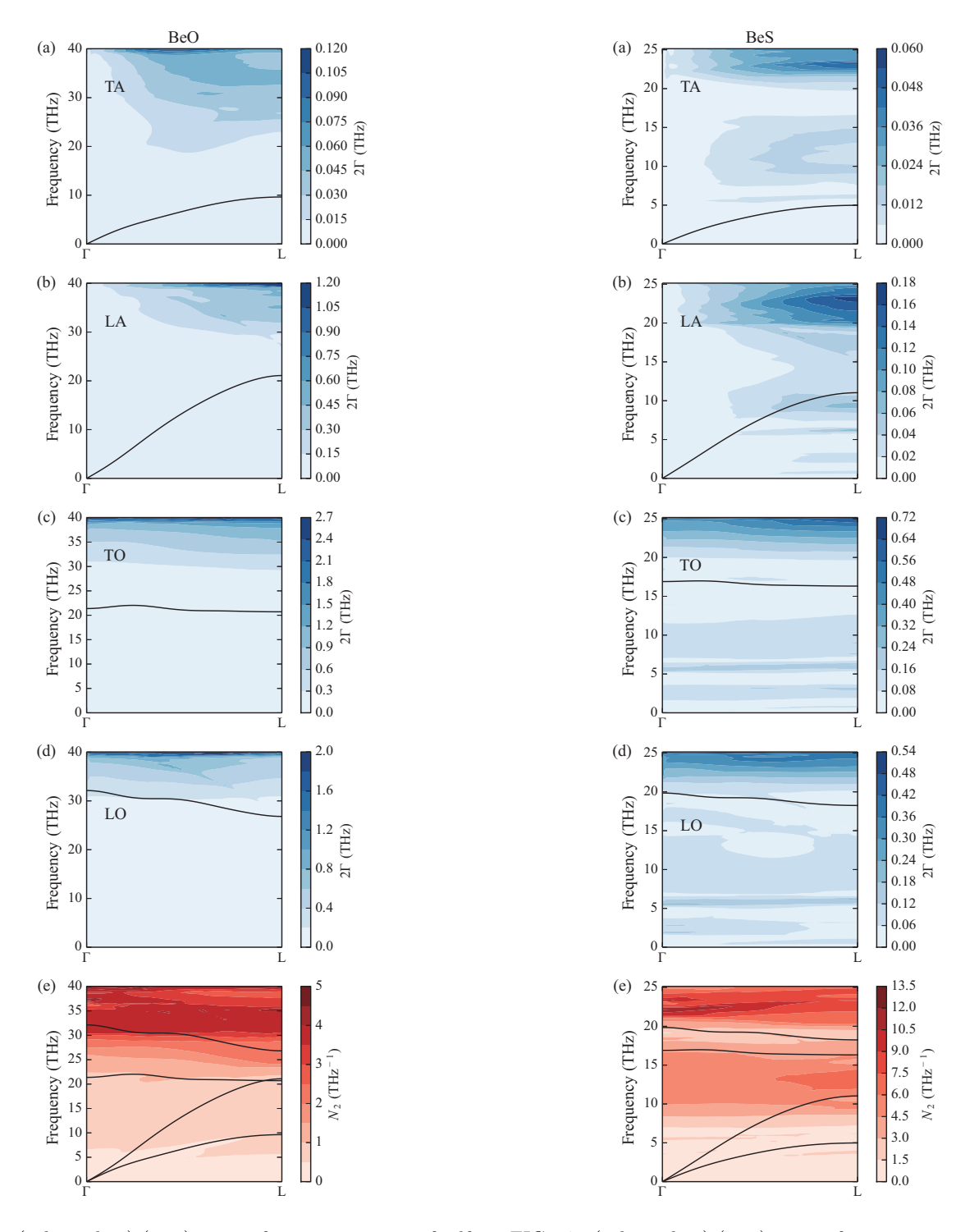


FIG. 36. (color online) (\mathbf{q}, ω) maps of imaginary parts of self energies $2\Gamma_{\lambda}(\omega)$ and w-JDOS $N_2(\mathbf{q}, \omega)$ of BeO.

FIG. 37. (color online) (\mathbf{q}, ω) maps of imaginary parts of self energies $2\Gamma_{\lambda}(\omega)$ and w-JDOS $N_2(\mathbf{q}, \omega)$ of BeS.

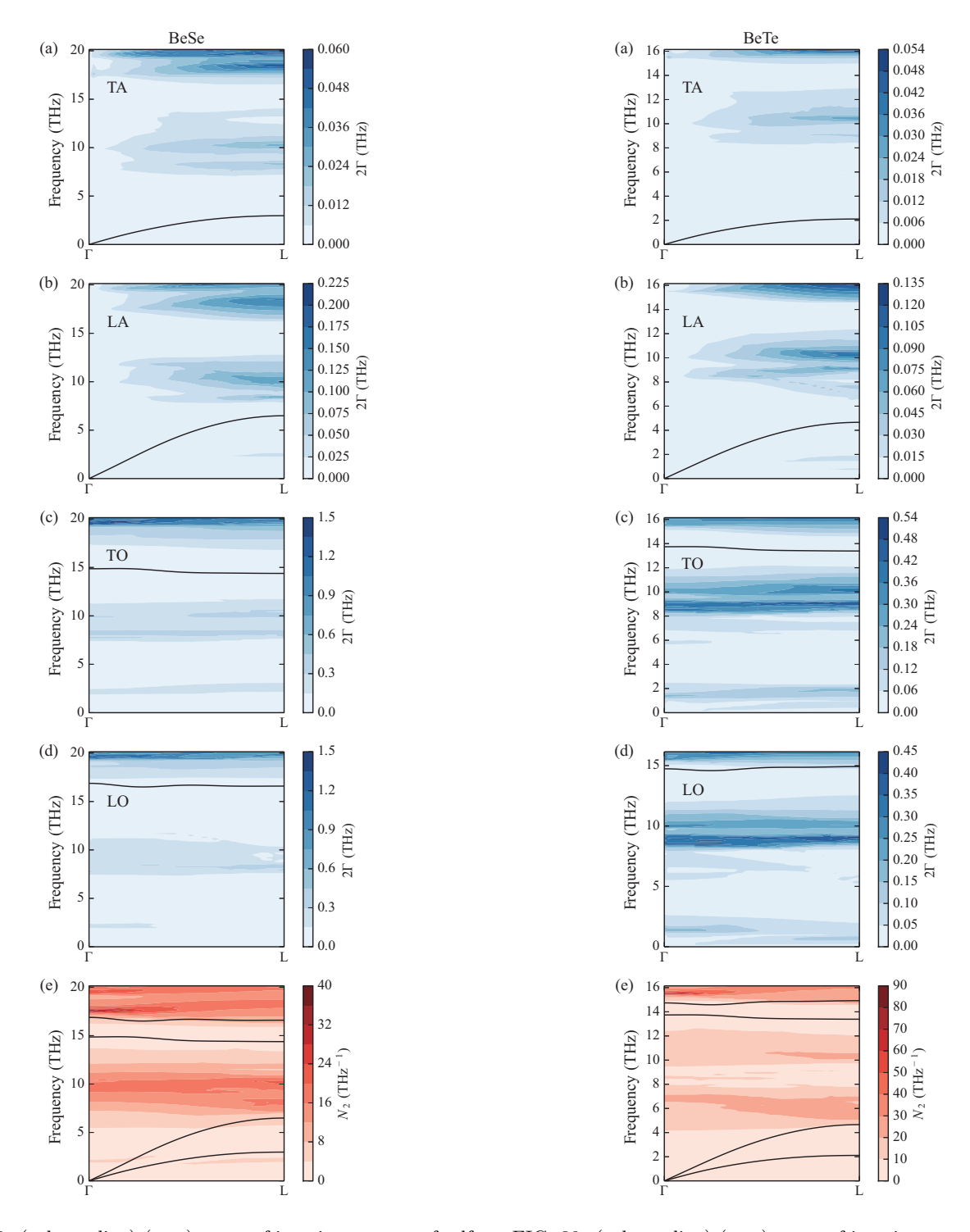


FIG. 38. (color online) (\mathbf{q}, ω) maps of imaginary parts of self energies $2\Gamma_{\lambda}(\omega)$ and w-JDOS $N_2(\mathbf{q}, \omega)$ of BeSe.

FIG. 39. (color online) (\mathbf{q}, ω) maps of imaginary parts of self energies $2\Gamma_{\lambda}(\omega)$ and w-JDOS $N_2(\mathbf{q}, \omega)$ of BeTe.

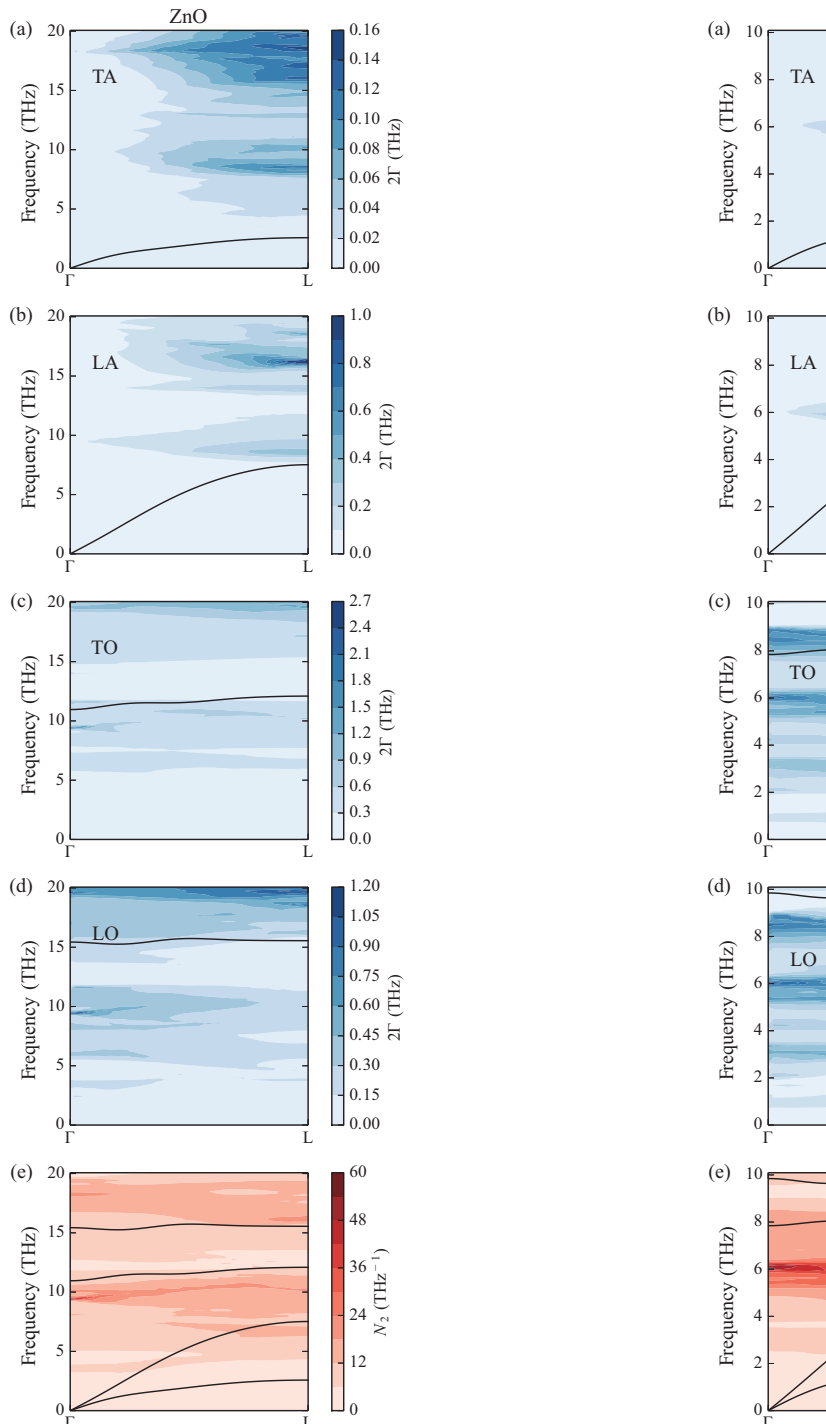


FIG. 40. (color online) (\mathbf{q}, ω) maps of imaginary parts of self energies $2\Gamma_{\lambda}(\omega)$ and w-JDOS $N_2(\mathbf{q}, \omega)$ of ZnO.

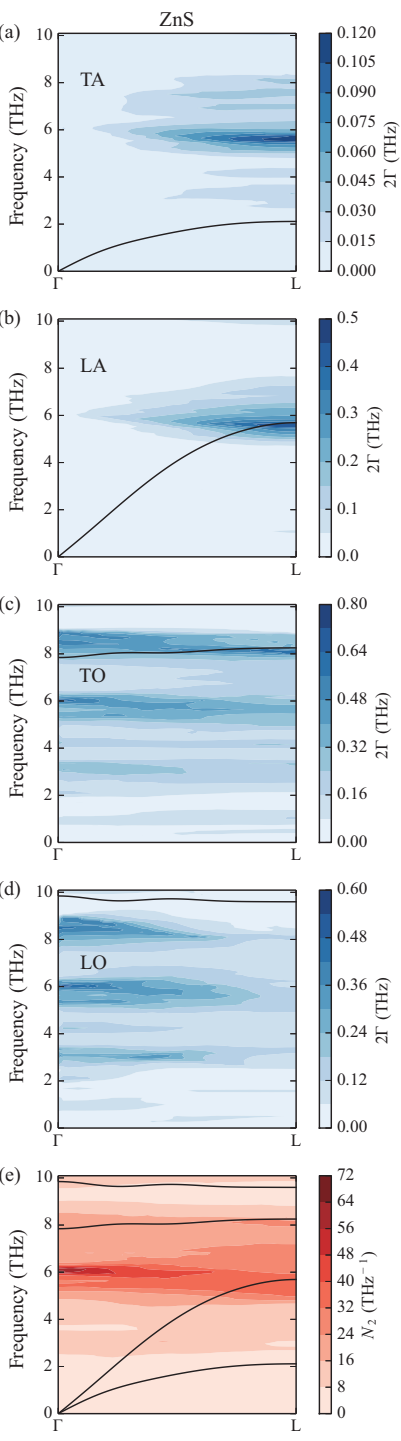


FIG. 41. (color online) (\mathbf{q}, ω) maps of imaginary parts of self energies $2\Gamma_{\lambda}(\omega)$ and w-JDOS $N_2(\mathbf{q}, \omega)$ of ZnS.

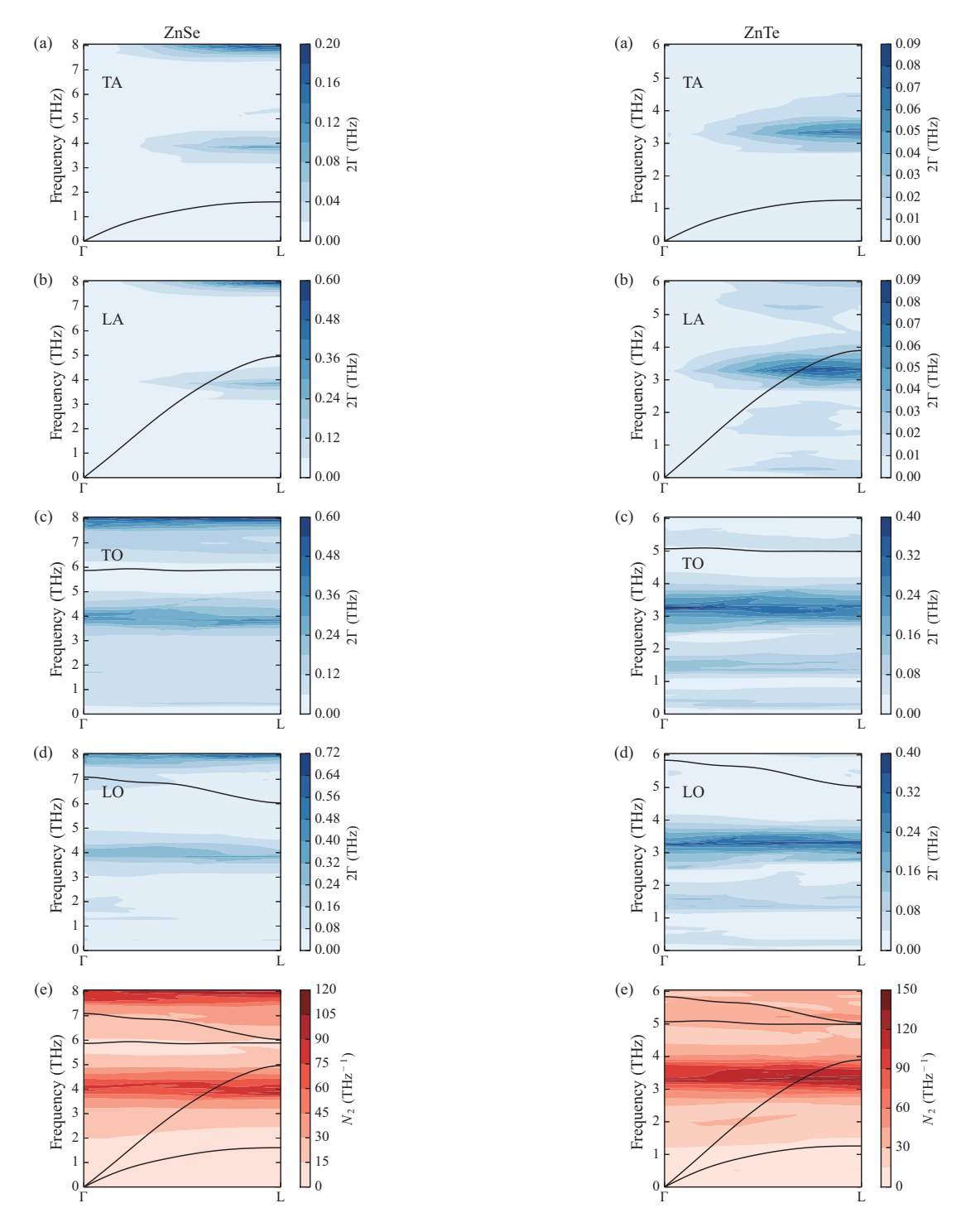


FIG. 42. (color online) (\mathbf{q}, ω) maps of imaginary parts of self energies $2\Gamma_{\lambda}(\omega)$ and w-JDOS $N_2(\mathbf{q}, \omega)$ of ZnSe.

FIG. 43. (color online) (\mathbf{q}, ω) maps of imaginary parts of self energies $2\Gamma_{\lambda}(\omega)$ and w-JDOS $N_2(\mathbf{q}, \omega)$ of ZnTe.

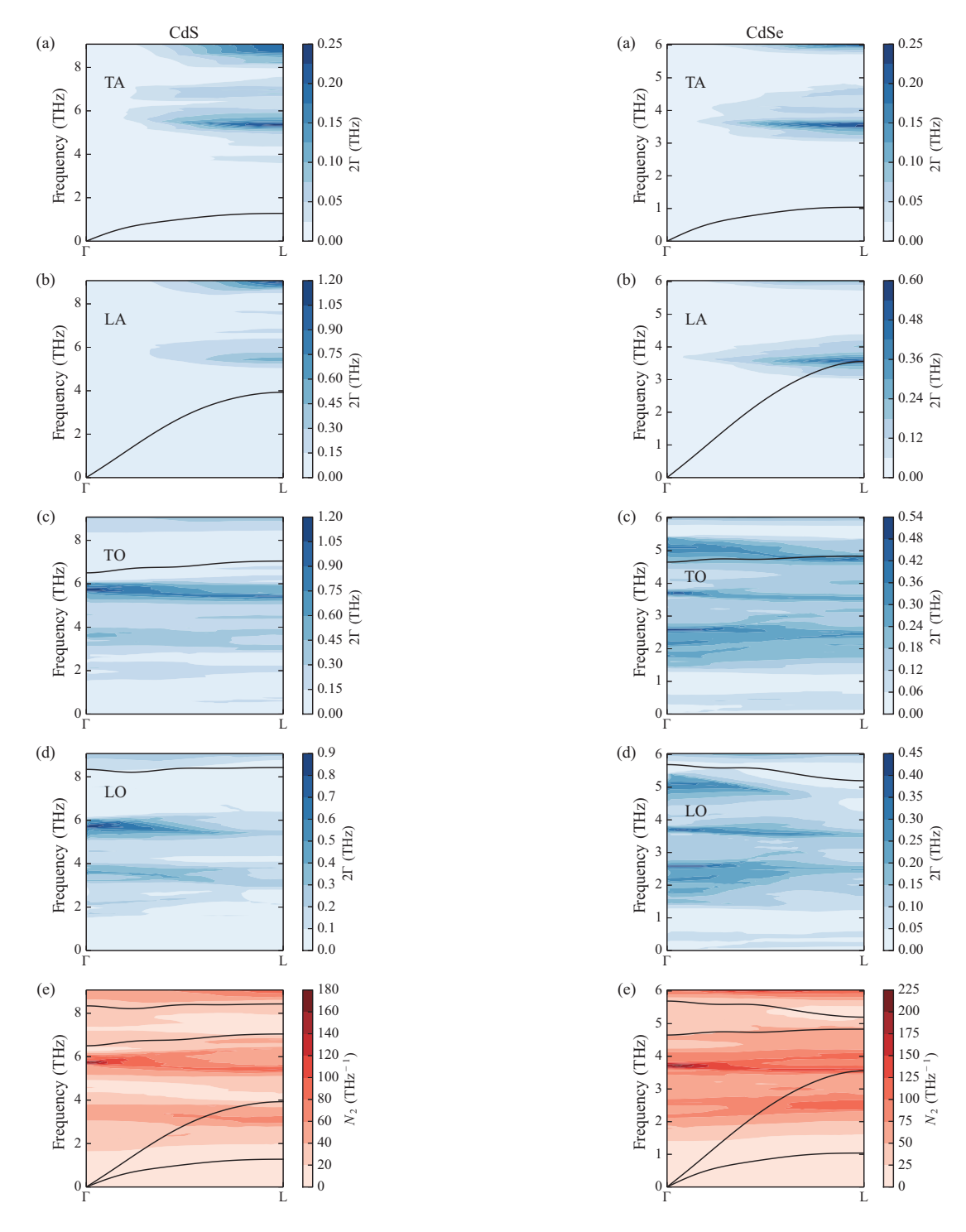


FIG. 44. (color online) (\mathbf{q}, ω) maps of imaginary parts of self energies $2\Gamma_{\lambda}(\omega)$ and w-JDOS $N_2(\mathbf{q}, \omega)$ of CdS.

FIG. 45. (color online) (\mathbf{q}, ω) maps of imaginary parts of self energies $2\Gamma_{\lambda}(\omega)$ and w-JDOS $N_2(\mathbf{q}, \omega)$ of CdSe.

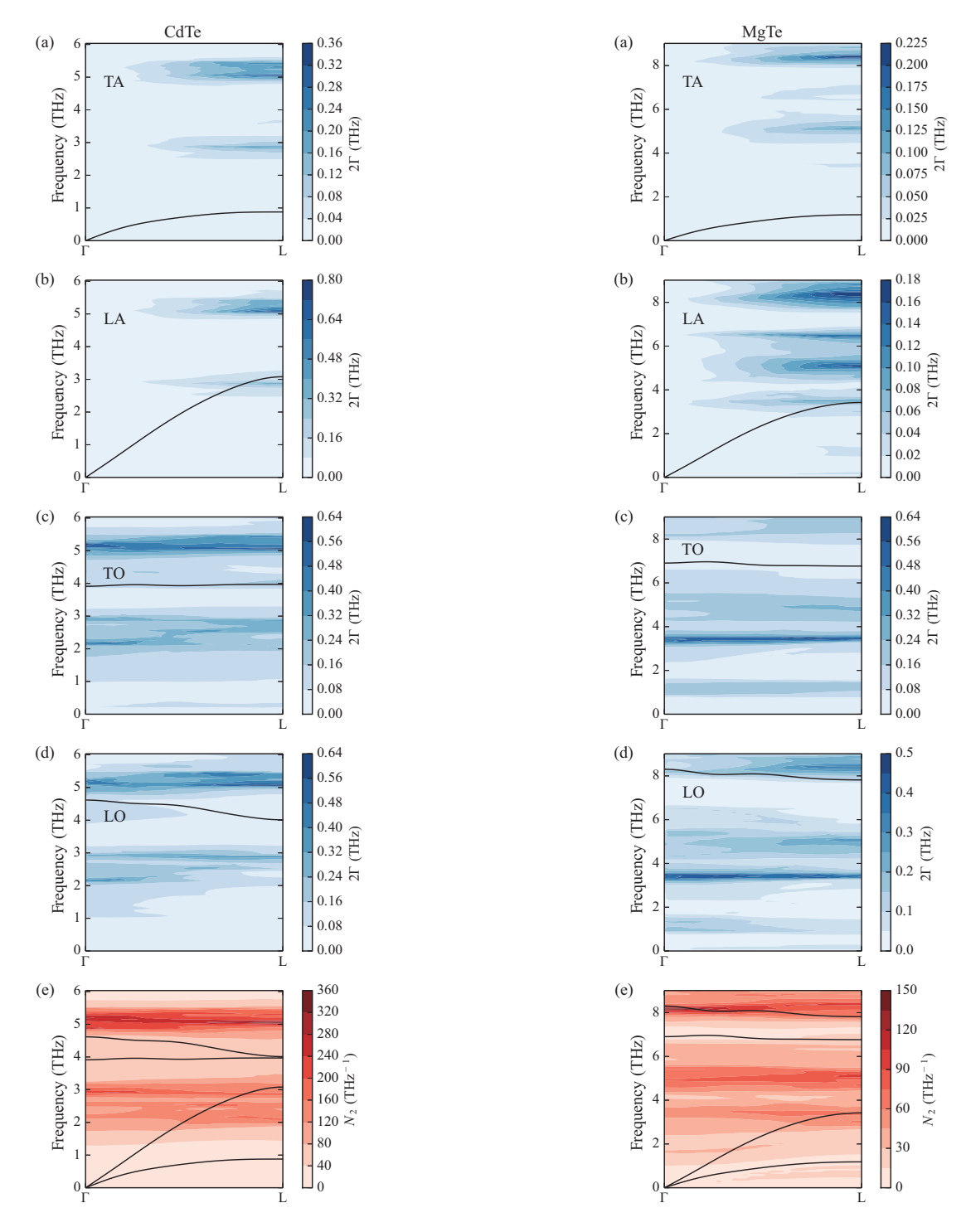


FIG. 46. (color online) (\mathbf{q}, ω) maps of imaginary parts of self energies $2\Gamma_{\lambda}(\omega)$ and w-JDOS $N_2(\mathbf{q}, \omega)$ of CdTe.

FIG. 47. (color online) (\mathbf{q}, ω) maps of imaginary parts of self energies $2\Gamma_{\lambda}(\omega)$ and w-JDOS $N_2(\mathbf{q}, \omega)$ of MgTe.

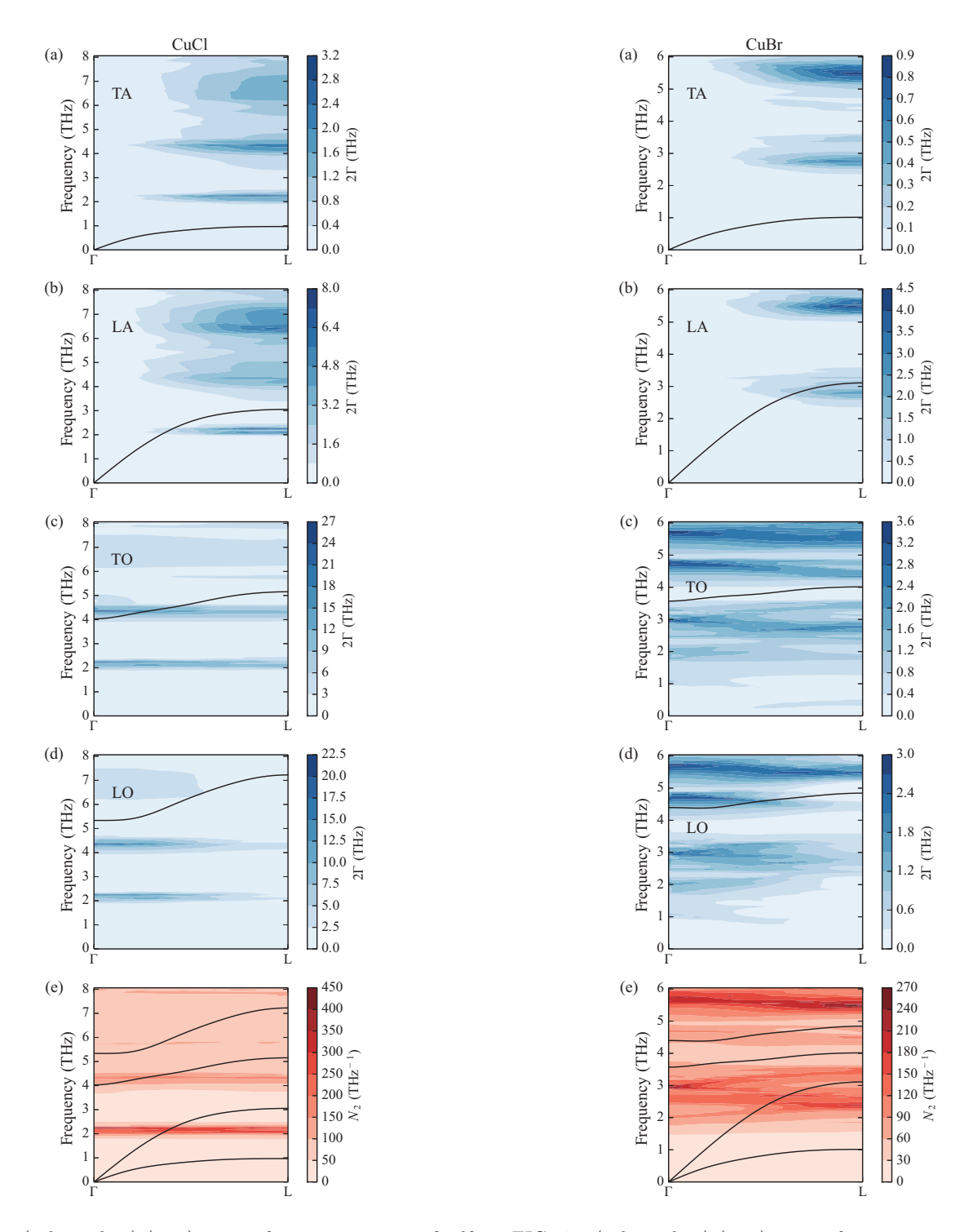


FIG. 48. (color online) (\mathbf{q}, ω) maps of imaginary parts of self energies $2\Gamma_{\lambda}(\omega)$ and w-JDOS $N_2(\mathbf{q}, \omega)$ of CuCl.

FIG. 49. (color online) (\mathbf{q}, ω) maps of imaginary parts of self energies $2\Gamma_{\lambda}(\omega)$ and w-JDOS $N_2(\mathbf{q}, \omega)$ of CuBr.

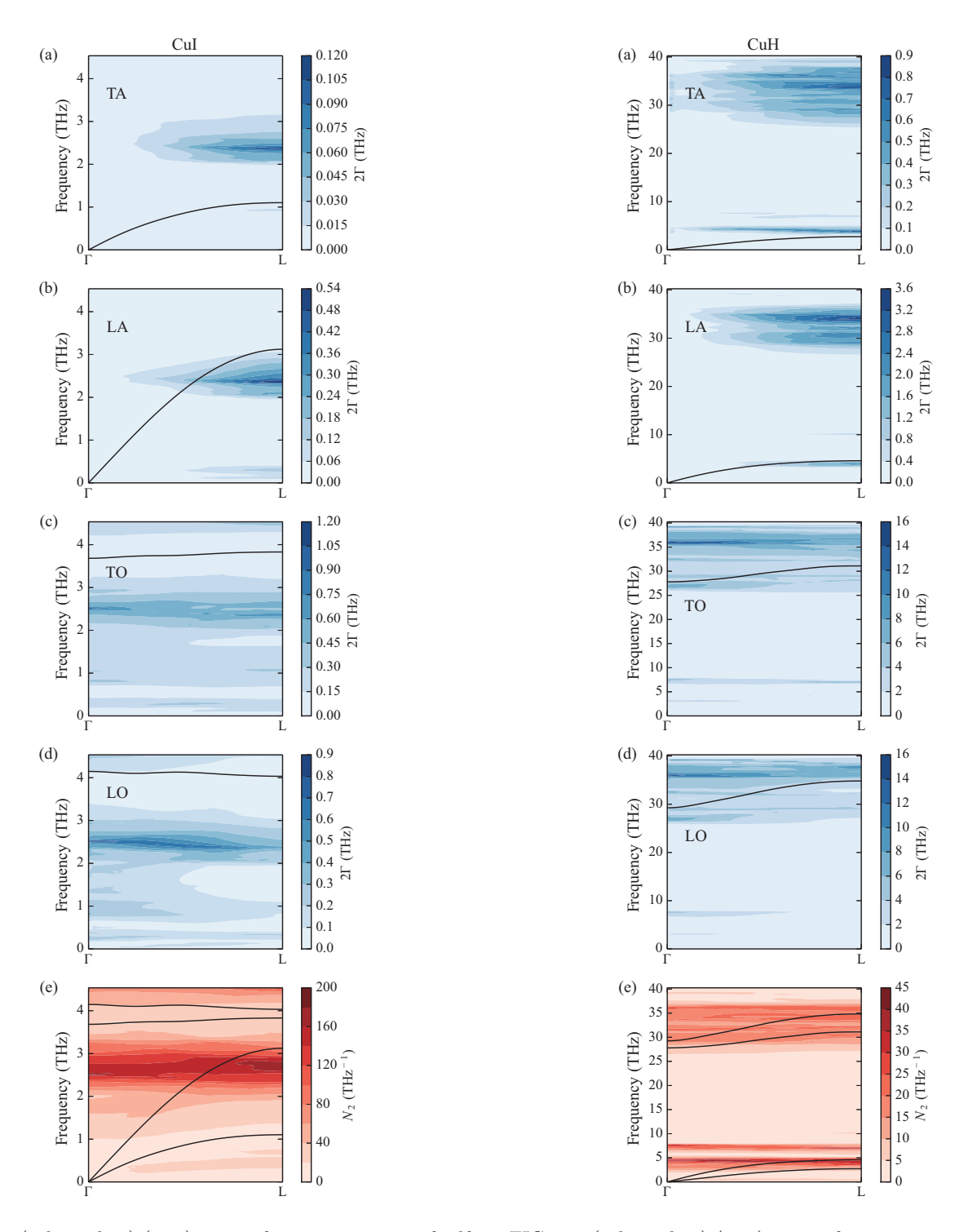


FIG. 50. (color online) (\mathbf{q}, ω) maps of imaginary parts of self energies $2\Gamma_{\lambda}(\omega)$ and w-JDOS $N_2(\mathbf{q}, \omega)$ of CuI.

FIG. 51. (color online) (\mathbf{q}, ω) maps of imaginary parts of self energies $2\Gamma_{\lambda}(\omega)$ and w-JDOS $N_2(\mathbf{q}, \omega)$ of CuH.

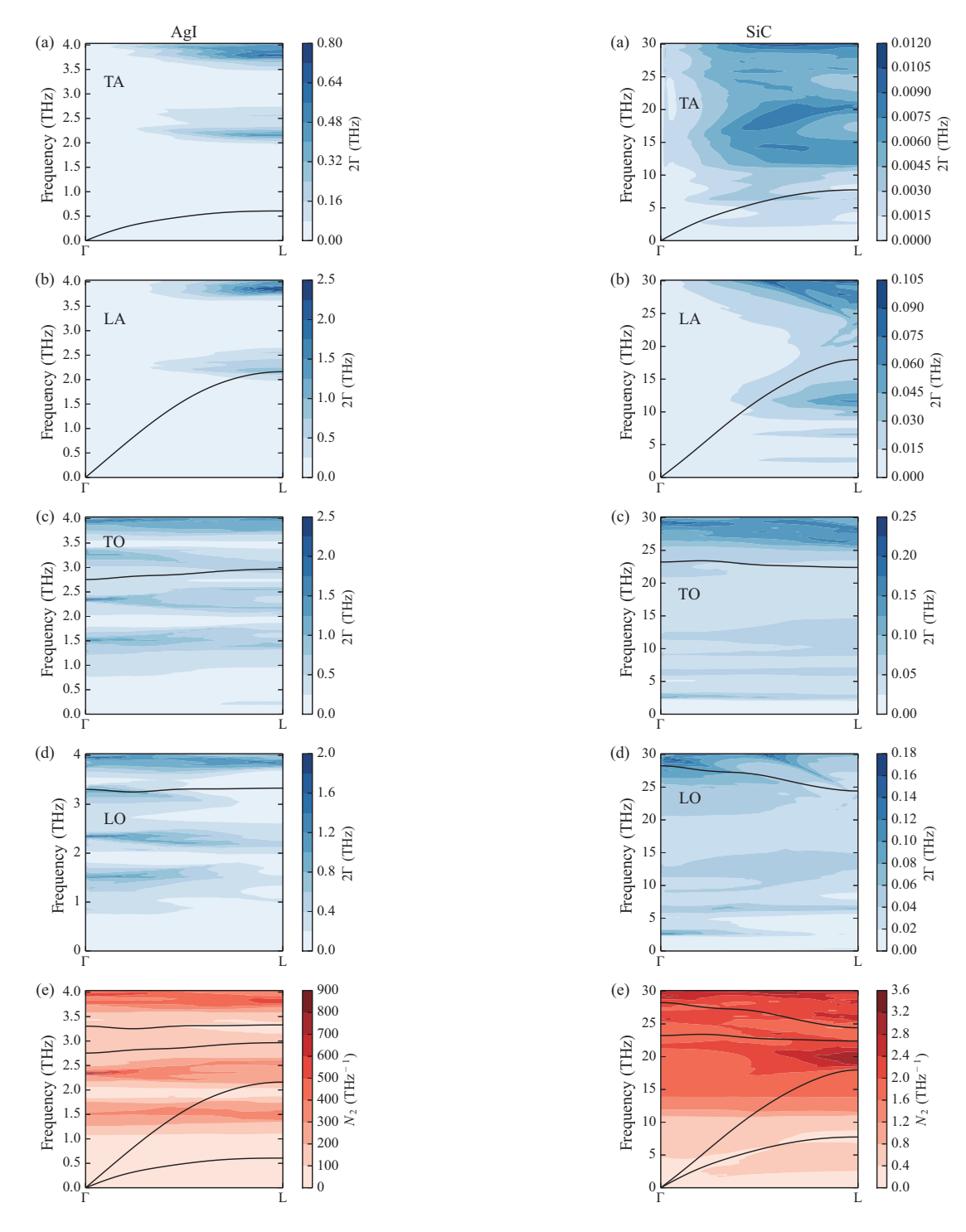


FIG. 52. (color online) (\mathbf{q}, ω) maps of imaginary parts of self energies $2\Gamma_{\lambda}(\omega)$ and w-JDOS $N_2(\mathbf{q}, \omega)$ of AgI.

FIG. 53. (color online) (\mathbf{q}, ω) maps of imaginary parts of self energies $2\Gamma_{\lambda}(\omega)$ and w-JDOS $N_2(\mathbf{q}, \omega)$ of SiC.

Appendix I: Lattice thermal conductivities

Lattice thermal conductivities of the 33 zincblende- and wurtzite-type compounds calculated with RTA and the method of the direct solution of LBTE¹ are listed in Tables III and IV. Scattering by the isotopes with the natural abundance³⁸ is considered in Table IV. Available experimental values in reports are shown in Table IV and comparisons between the experiments and calculations are graphically shown in Fig. 2. The methods to include isotope effect and the direct solution of LBTE are described in Appendices D and E, respectively.

TABLE III. Calculated lattice thermal conductivities of the 33 zincblende- and wurtzite-type compounds at 300 K in W/m-K.

	Zincbler	nde-type	Wurtzite-type				
	RTA	LBTE	R	ГА	LB	TE	
	xx	xx	xx	zz	xx	zz	
BN	1.17×10^{3}	1.80×10^{3}	9.30×10^{2}	9.24×10^{2}	1.23×10^{3}	1.04×10^{3}	
BP	4.27×10^{2}	4.64×10^{2}	4.18×10^{2}	3.19×10^{2}	4.31×10^{2}	3.28×10^2	
BAs	1.59×10^{3}	5.61×10^{3}	1.44×10^{3}	1.09×10^{3}	2.38×10^{3}	1.21×10^3	
AlN	2.12×10^{2}	2.35×10^{2}	2.24×10^{2}	2.07×10^{2}	2.40×10^{2}	2.12×10^2	
AlP	8.30×10^{1}	8.40×10^{1}	7.48×10^{1}	7.14×10^{1}	7.46×10^{1}	7.17×10^1	
AlAs	8.56×10^{1}	8.68×10^{1}	7.23×10^{1}	6.96×10^{1}	7.39×10^{1}	7.10×10^{1}	
AlSb	8.92×10^{1}	9.48×10^{1}	6.18×10^{1}	5.84×10^{1}	6.35×10^{1}	5.82×10^1	
GaN	2.31×10^{2}	3.37×10^{2}	2.56×10^{2}	2.38×10^{2}	2.73×10^{2}	2.66×10^{2}	
GaP	9.62×10^{1}	1.22×10^{2}	1.04×10^{2}	9.08×10^{1}	1.11×10^{2}	9.63×10^{1}	
GaAs	3.18×10^{1}	3.31×10^{1}	2.85×10^{1}	2.61×10^{1}	2.86×10^{1}	2.66×10^{1}	
GaSb	3.30×10^{1}	3.39×10^{1}	2.42×10^{1}	1.97×10^{1}	2.48×10^{1}	2.02×10^{1}	
InN	9.54×10^{1}	1.08×10^{2}	1.10×10^{2}	1.13×10^{2}	1.18×10^{2}	1.19×10^2	
InP	7.51×10^{1}	8.71×10^{1}	6.87×10^{1}	6.57×10^{1}	7.02×10^{1}	6.93×10^{1}	
InAs	2.05×10^{1}	2.53×10^{1}	1.83×10^{1}	1.71×10^{1}	1.86×10^{1}	1.80×10^1	
InSb	$1.27{\times}10^{1}$	1.40×10^{1}	9.71×10^{0}	9.63×10^{0}	9.83×10^{0}	9.93×10^{0}	
BeO	3.58×10^{2}	4.64×10^{2}	2.86×10^{2}	2.98×10^{2}	3.36×10^{2}	3.20×10^{2}	
BeS	1.57×10^{2}	1.74×10^{2}	1.29×10^{2}	1.21×10^2	1.37×10^{2}	1.27×10^2	
BeSe	3.89×10^{2}	6.75×10^2	3.21×10^{2}	3.12×10^2	4.08×10^2	3.36×10^2	
BeTe	2.86×10^{2}	5.03×10^2	1.83×10^{2}	1.82×10^{2}	2.36×10^2	1.93×10^2	
MgTe	1.57×10^{1}	$1.57{\times}10^{1}$	1.22×10^{1}	1.36×10^{1}	1.24×10^1	1.35×10^1	
ZnO	5.82×10^{1}	8.93×10^{1}	4.63×10^{1}	6.24×10^{1}	4.66×10^{1}	6.48×10^{1}	
ZnS	3.72×10^{1}	4.72×10^{1}	3.73×10^{1}	4.03×10^{1}	3.89×10^{1}	4.69×10^{1}	
ZnSe	1.63×10^{1}	1.72×10^{1}	1.50×10^{1}	1.53×10^{1}	1.51×10^{1}	1.57×10^1	
ZnTe	1.96×10^{1}	2.04×10^{1}	1.45×10^{1}	1.55×10^{1}	1.45×10^{1}	1.58×10^1	
CdS	2.13×10^{1}	2.30×10^{1}	1.79×10^{1}	2.01×10^1	1.88×10^{1}	2.05×10^1	
CdSe	1.10×10^{1}	1.24×10^{1}	8.86×10^{0}	9.58×10^{0}	8.81×10^{0}	1.04×10^{1}	
CdTe	6.51×10^{0}	6.95×10^{0}	5.03×10^{0}	5.67×10^{0}	5.01×10^{0}	5.87×10^{0}	
CuCl	1.48×10^{0}	1.11×10^{0}	1.01×10^{0}	1.75×10^{0}	1.04×10^{0}	2.02×10^{0}	
CuBr	2.55×10^{0}	2.79×10^{0}	1.77×10^{0}	2.88×10^{0}	1.75×10^{0}	3.04×10^{0}	
CuI	6.53×10^{0}	7.22×10^{0}	5.89×10^{0}	6.94×10^{0}	6.07×10^{0}	7.32×10^{0}	
CuH	1.44×10^{1}	1.50×10^{1}	8.17×10^{0}	6.47×10^0	8.62×10^{0}	8.12×10^0	
AgI	2.02×10^{0}	2.47×10^{0}	1.39×10^{0}	1.78×10^{0}	1.38×10^{0}	1.90×10^{0}	
SiC	4.15×10^{2}	4.42×10^{2}	4.05×10^2	3.44×10^2	4.20×10^2	3.48×10^2	

TABLE IV. Calculated lattice thermal conductivities of the 33 zincblende- and wurtzite-type compounds with isotope effect at 300 K in W/m-K. Experimental values at room temperature are also presented.

	Zincblende-type			Wurtzite-type				
	RTA LBTE		Exp.	RT	RTA		LBTE	
	xx	xx		xx	zz	xx	zz	
BN	6.48×10^2	7.26×10^{2}	7.6×10^{2} a	5.61×10^{2}	5.42×10^{2}	6.02×10^{2}	5.73×10^{2}	-
BP	3.96×10^{2}	4.20×10^{2}	3.5×10^{2} a	3.89×10^{2}	3.01×10^2	3.95×10^2	3.07×10^2	-
BAs	1.23×10^{3}	2.94×10^{3}	-	1.15×10^3	9.07×10^2	1.73×10^3	9.94×10^2	-
AlN	2.11×10^{2}	2.35×10^{2}	-	2.24×10^2	2.07×10^2	2.39×10^2	2.12×10^2	3.5×10^{2} a
AlP	8.30×10^{1}	8.40×10^{1}	$9 \times 10^{1} ^{\rm b}$	7.48×10^{1}	7.14×10^1	7.46×10^{1}	7.17×10^1	-
AlAs	8.56×10^{1}	8.68×10^{1}	9.8×10^{1} a	7.23×10^{1}	6.96×10^{1}	7.39×10^{1}	7.10×10^{1}	-
AlSb	7.51×10^{1}	7.74×10^{1}	5.6×10^{1} a	5.71×10^{1}	5.44×10^1	5.82×10^1	5.40×10^{1}	-
GaN	1.54×10^{2}	1.81×10^{2}	-	1.65×10^{2}	1.66×10^2	1.71×10^2	1.72×10^2	$2.1{\times}10^{2~\mathrm{a}}$
GaP	8.55×10^{1}	1.04×10^{2}	1.00×10^{2} a	9.19×10^{1}	8.16×10^{1}	9.65×10^{1}	8.54×10^{1}	-
GaAs	3.10×10^{1}	3.21×10^{1}	4.5×10^{1} a	2.78×10^{1}	2.55×10^1	2.78×10^{1}	2.59×10^{1}	-
GaSb	3.18×10^{1}	3.25×10^{1}	4×10^{1} a	2.34×10^{1}	1.92×10^{1}	2.39×10^{1}	1.96×10^{1}	-
InN	9.31×10^{1}	1.05×10^{2}	-	1.06×10^{2}	1.10×10^2	1.14×10^2	1.16×10^2	-
InP	7.38×10^{1}	8.52×10^{1}	9.3×10^{1} a	6.78×10^{1}	6.49×10^1	6.93×10^{1}	6.82×10^1	-
InAs	2.04×10^{1}	2.52×10^{1}	3×10^{1} a	1.83×10^{1}	1.70×10^{1}	1.85×10^1	1.80×10^{1}	-
InSb	1.26×10^{1}	1.38×10^{1}	2×10^{1} a	9.64×10^{0}	9.56×10^{0}	9.76×10^{0}	9.86×10^{0}	-
${\rm BeO}$	3.50×10^{2}	4.47×10^{2}	-	2.80×10^{2}	2.93×10^2	3.27×10^2	3.14×10^2	3.7×10^{2} a
BeS	1.43×10^{2}	1.57×10^{2}	-	1.19×10^{2}	1.12×10^2	1.26×10^2	1.18×10^2	-
BeSe	9.50×10^{1}	1.08×10^{2}	-	7.57×10^{1}	8.02×10^{1}	8.19×10^{1}	8.31×10^1	-
BeTe	7.75×10^{1}	9.04×10^{1}	-	6.41×10^{1}	6.07×10^1	7.10×10^{1}	6.29×10^{1}	-
MgTe	1.48×10^{1}	1.47×10^{1}	-	1.14×10^{1}	1.27×10^1	1.16×10^1	1.27×10^{1}	-
ZnO	5.04×10^{1}	6.45×10^{1}	-	4.10×10^{1}	5.56×10^1	4.13×10^{1}	5.73×10^1	6×10^{1} a
ZnS	3.10×10^{1}	3.65×10^{1}	2.7×10^{1} a	3.15×10^{1}	3.40×10^{1}	3.24×10^{1}	3.83×10^{1}	-
ZnSe	1.49×10^{1}	1.56×10^{1}	1.9×10^{1} a	1.37×10^{1}	1.42×10^{1}	1.38×10^1	1.45×10^1	-
ZnTe	1.84×10^{1}	1.89×10^{1}	1.8×10^{1} a	1.38×10^{1}	1.48×10^{1}	1.38×10^1	1.51×10^{1}	-
CdS	1.90×10^{1}	1.99×10^{1}	-	1.61×10^{1}	1.83×10^{1}	1.66×10^{1}	1.85×10^{1}	1.6×10^{1} a
CdSe	1.03×10^{1}	1.14×10^{1}	-	8.42×10^{0}	9.16×10^{0}	8.37×10^{0}	9.87×10^{0}	-
CdTe	6.28×10^{0}	6.67×10^{0}	7.5×10^{0} a	4.90×10^{0}	5.52×10^0	4.87×10^{0}	5.71×10^{0}	-
CuCl	1.44×10^{0}	1.26×10^{0}	-	9.95×10^{-1}	1.71×10^{0}	1.02×10^{0}	1.97×10^{0}	8.4×10^{-1} c
CuBr	2.52×10^{0}	2.75×10^{0}	-	1.76×10^{0}	2.83×10^{0}	1.74×10^{0}	2.99×10^{0}	$1.25{ imes}10^{0} { m c}$
CuI	6.45×10^{0}	7.10×10^{0}	-	5.82×10^{0}	6.85×10^{0}	5.99×10^{0}	7.22×10^{0}	1.68×10^{0} c
CuH	1.39×10^{1}	1.44×10^{1}	-	7.81×10^{0}	6.16×10^{0}	8.22×10^0	7.60×10^0	-
AgI	2.01×10^{0}	2.44×10^{0}	-	1.38×10^{0}	1.78×10^{0}	1.37×10^{0}	1.89×10^{0}	1.03×10^{0} d
SiC	3.55×10^{2}	3.72×10^{2}	-	3.55×10^2	3.11×10^{2}	3.67×10^2	3.14×10^{2}	4.9×10^{2} a

^a Ref. 39. ^b Ref. 40. ^c Ref. 41. ^d Ref. 42.

- * togo.atsushi@gmail.com
- ¹ L. Chaput, Phys. Rev. Lett. **110**, 265506 (2013).
- ² D. A. Broido, M. Malorny, G. Birner, N. Mingo, and D. A. Stewart, Applied Physics Letters 91, 231922 (2007).
- ³ A. Ward and D. A. Broido, Phys. Rev. B **77**, 245328 (2008).
- ⁴ A. Ward, D. A. Broido, D. A. Stewart, and G. Deinzer, Phys. Rev. B 80, 125203 (2009).
- ⁵ A. Ward and D. A. Broido, Phys. Rev. B **81**, 085205 (2010).
- ⁶ K. Esfarjani, G. Chen, and H. T. Stokes, Phys. Rev. B 84, 085204 (2011).
- ⁷ J. Shiomi, K. Esfarjani, and G. Chen, Phys. Rev. B 84, 104302 (2011).
- ⁸ Z. Tian, J. Garg, K. Esfarjani, T. Shiga, J. Shiomi, and G. Chen, Phys. Rev. B **85**, 184303 (2012).
- ⁹ T. Shiga, J. Shiomi, J. Ma, O. Delaire, T. Radzynski, A. Lusakowski, K. Esfarjani, and G. Chen, Phys. Rev. B 85, 155203 (2012).
- ¹⁰ L. Lindsay, D. A. Broido, and T. L. Reinecke, Phys. Rev. Lett. **109**, 095901 (2012).
- ¹¹ L. Lindsay, D. A. Broido, and T. L. Reinecke, Phys. Rev. B 87, 165201 (2013).
- L. Lindsay, D. A. Broido, and T. L. Reinecke, Phys. Rev. B 88, 144306 (2013).
- ¹³ L. Lindsay, D. A. Broido, and T. L. Reinecke, Phys. Rev. Lett. **111**, 025901 (2013).
- ¹⁴ A. van de Walle and G. Ceder, Rev. Mod. Phys. **74**, 11 (2002).
- A. Alam and A. Mookerjee, Phys. Rev. B 69, 024205 (2004).
- A. Alam and A. Mookerjee, Phys. Rev. B 71, 094210 (2005).
- ¹⁷ A. Alam and A. Mookerjee, Phys. Rev. B **72**, 214207 (2005).
- ¹⁸ D. C. Wallace, <u>Thermodynamics of crystals</u> (Dover Publications, 1998).
- ¹⁹ A. A. Maradudin and A. E. Fein, Phys. Rev. **128**, 2589 (1962).
- ²⁰ G. P. Srivastava, Physics of phonons (CRC Press, 1990).

- ²¹ L. Chaput, A. Togo, I. Tanaka, and G. Hug, Phys. Rev. B 84, 094302 (2011).
- ²² R. M. Pick, M. H. Cohen, and R. M. Martin, Phys. Rev. B 1, 910 (1970).
- ²³ Y. Wang, J. J. Wang, W. Y. Wang, Z. G. Mei, S. L. Shang, L. Q. Chen, and Z. K. Liu, J. Phys.: Condens. Matter 22, 202201 (2010).
- ²⁴ P. E. Blöchl, Phys. Rev. B **50**, 17953 (1994).
- ²⁵ G. Kresse, J. Non-Cryst. Solids **193**, 222 (1995).
- ²⁶ G. Kresse and J. Furthmüller, Comput. Mater. Sci. 6, 15 (1996).
- ²⁷ G. Kresse and D. Joubert, Phys. Rev. B **59**, 1758 (1999).
- ²⁸ J. P. Perdew, K. Burke, and M. Ernzerhof, Phys. Rev. Lett. **77**, 3865 (1996).
- ²⁹ M. Gajdoš, K. Hummer, G. Kresse, J. Furthmüller, and F. Bechstedt, Phys. Rev. B 73, 045112 (2006).
- ³⁰ X. Wu, D. Vanderbilt, and D. R. Hamann, Phys. Rev. B 72, 035105 (2005).
- ³¹ X. Gonze and C. Lee, Phys. Rev. B **55**, 10355 (1997).
- ³² A. H. MacDonald, S. H. Vosko, and P. T. Coleridge, Journal of Physics C: Solid State Physics 12, 2991 (1979).
- ³³ P. E. Blöchl, O. Jepsen, and O. K. Andersen, Phys. Rev. B 49, 16223 (1994).
- ³⁴ T. Tadano, Y. Gohda, and S. Tsuneyuki, J. Phys.: Condens. Matter **26**, 225402 (2014).
- ³⁵ W. Cochran and R. A. Cowley, J. Phys. Chem. Solids 23, 447 (1962).
- ³⁶ P. Giannozzi, S. de Gironcoli, P. Pavone, and S. Baroni, Phys. Rev. B 43, 7231 (1991).
- ³⁷ S.-i. Tamura, Phys. Rev. B **27**, 858 (1983).
- ³⁸ J. R. de Laeter, J. K. Böhlke, P. De Bièvre, H. Hidaka, H. S. Peiser, K. J. R. Rosman, and P. D. P. Taylor, Pure Appl. Chem. **75**, 683 (2003).
- ³⁹ S. L. Shiné and J. S. Goela, High thermal conductivity materials (Springer, 2006).
- ⁴⁰ E. F. Steigmeier and I. Kudman, Phys. Rev. **141**, 767 (1966).
- ⁴¹ D. L. Perry, <u>Handbook of Inorganic Compounds</u>, <u>Second Edition</u> (CRC Press, 2011).
- ⁴² M. C. Goetz and J. A. Cowen, Solid State Communications 41, 293 (1982).